JGR Planets

RESEARCH ARTICLE
10.1029/2020JE006485

Special Section:
5th International Planetary Dunes Workshop Special Issue

This article is a companion to Lorenz (2020), https://doi.org/10.1029/2020JE006658.

A Broad Continuum of Aeolian Impact Ripple Morphologies on Mars is Enabled by Low Wind Dynamic Pressures

R. Sullivan[1], J. F. Kok[2], I. Katra[3], and H. Yizhaq[4]

[1]Cornell Center for Astrophysics and Planetary Sciences, Cornell University, Ithaca, NY, USA, [2]Department of Atmospheric and Oceanic Sciences, University of California, Los Angeles, Los Angeles, CA, USA, [3]Department of Geography and Environmental Development, Ben-Gurion University of the Negev, Beer Sheva, Israel, [4]Department of Solar Energy and Environmental Physics, BIDR, Ben-Gurion University of the Negev, Beer Sheva, Israel

Abstract Aeolian ripples are common in sandy environments on Earth and Mars. On Earth, ripples in sorted dune sands typically are <1 cm high and are erased in high winds. On Mars in similar sands, ripple wavelengths commonly exceed 2 m, with much smaller ripples superimposed. Large Martian ripple sizes and juxtaposition of multiple wavelengths have raised questions about origins and the applicability of terrestrial aeolian physics to different planetary environments. Here, two hypotheses are evaluated for large Martian ripples: (1) fluid/wind drag, analogous to ripples formed under water on Earth, as proposed previously for Martian large ripples; and (2) saltation impact splash, the mechanism creating aeolian ripples of much smaller size on Earth. This study evaluates these hypotheses with numerical experiments and Mars rover observations, and concludes that large Martian ripples develop through the saltation impact splash mechanism. The low-density Martian atmosphere enables aeolian impact ripples to grow much higher into the boundary layer before reaching maximum heights constrained by wind dynamic pressure effects at crests. In this concept, boundary layer conditions influence mature ripple heights more directly than wavelengths. On Mars, low wind dynamic pressures, combined with the impact splash mechanism, also help to explain other distinctively Martian aeolian bedforms, including large longitudinal ripples observed by rovers and orbiters, and transverse aeolian ridges (TARs) distributed widely across the Martian surface. Compared with Earth, low wind dynamic pressures on Mars permit a wider range of ripple sizes, relative ages, morphologies, and orientations in close proximity, as displayed in rover observations.

Plain Language Summary On Earth, winds drive sand grains downwind in bouncing motions (called "saltation"). Each high-energy bounce also splashes other surface grains shorter distances, and this impact splash process creates small, ~10 cm wavelength ripples with heights <1 cm in typical dune sands. On Mars, sands with similar grain sizes form much larger ripples with wavelengths exceeding 2 m, and their origins have been debated. In this study, numerical simulations and Mars rover observations indicate that aeolian impact ripples can grow much larger on Mars than on Earth because the thin Martian atmosphere does not interfere with the upward growth of ripple crests until ripples are much higher (which in turn constrains minimum, but not maximum, ripple wavelengths). In this concept, wind conditions influence mature aeolian ripple heights more directly than ripple wavelengths. This concept also helps explain other, distinctively Martian aeolian features including large longitudinal ripples, and large transverse aeolian ridges (TARs) observed widely across the Martian surface.

Key Points:
- On Mars, the saltation impact splash mechanism creates a wider range of aeolian ripple sizes than on Earth
- Low wind dynamic pressures on Mars allow ripple heights to grow further upward into the boundary layer than on Earth
- The same mechanism also helps explain other distinctively Martian bedforms: large longitudinal ripples and transverse aeolian ridges (TARs)

Correspondence to:
R. Sullivan,
rjs33@cornell.edu

Citation:
Sullivan, R., Kok, J. F., Katra, I., & Yizhaq, H. (2020). A broad continuum of aeolian impact ripple morphologies on Mars is enabled by low wind dynamic pressures. *Journal of Geophysical Research: Planets*, *125*, e2020JE006485. https://doi.org/10.1029/2020JE006485

Received 28 APR 2020
Accepted 19 AUG 2020
Accepted article online 25 AUG 2020

1. Introduction

Ripples are common bedforms of arid, sandy environments. Vast arrays of ripples with ~10 cm wavelengths are distributed across the surfaces of sand dunes in terrestrial deserts (Figure 1). The ubiquity of aeolian ripples, their importance in the rock record for interpreting past environments, and their intriguing, repeating geometrical form have motivated many investigations into factors controlling ripple development, shape, and size (e.g., Anderson, 1990; Andreotti et al., 2006; Bagnold, 1941, pp. 144–166; Cheng et al., 2018; Durán et al., 2011, 2014; Ellwood et al., 1975; Manukyan & Prigozhin, 2009; Pelletier, 2009; Rasmussen et al., 2015; Schmerler et al., 2016; Sharp, 1963; Walker, 1981). Nevertheless, the physics of aeolian ripples has proven to be more complex than their simple forms might initially suggest, and uncertainties remain

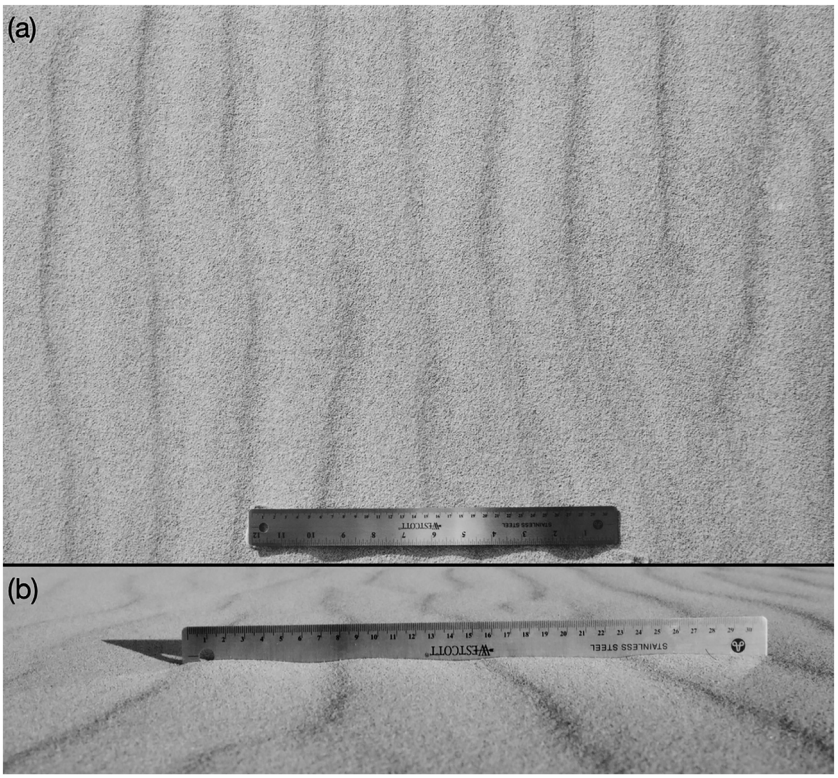

Figure 1. Example terrestrial impact ripples from two locations at Kelso dunes, CA. (a) Impact ripples with wavelength λ ~ 7.5 cm. Illumination from upper left. (b) Impact ripples showing asymmetric profiles, indicating migration right to left. Illumination from right. Average λ ~ 7.8 cm, average height h is ~0.2 cm, so ripple index RI ~ 39.

about how environmental factors combine to control ripple wavelength, size, and morphology (Andreotti et al., 2006; Durán et al., 2011; McKenna Neuman & Bédard, 2016).

Ripples are also abundant in sandy areas of Mars, a planet with 38% of Earth's gravity and <1% of Earth's atmospheric surface pressure. Surprisingly, ripples on Mars can grow an order of magnitude larger than their terrestrial counterparts with similar grain size frequencies (e.g., Bridges et al., 2007; Lapotre et al., 2016; Sullivan et al., 2008; Vaz et al., 2017) (Figure 2). These very large Martian ripples have been interpreted as outsized analogs of smaller, familiar aeolian ripples on Earth (Sullivan et al., 2008), but without explanation of how aeolian saltation could produce much larger ripples in the Martian environment. An alternative view is that long Martian ripple wavelengths are controlled by the same mechanism controlling subaqueous current ripples on Earth (different mechanisms proposed by Duran Vinent et al., 2019; Lapotre et al., 2016; Lapotre & Rampe, 2018). Evaluating origins of these bedforms is the purpose of this paper, which uses a standard Multiple Working Hypotheses approach (Chamberlin, 1897). At stake in this evaluation is whether very large ripples on Mars represent: (1) an important learning ground for testing and applying fundamental aeolian physics in an environment different from Earth; or (2) an extension of terrestrial subaqueous bedform physics to the exotic subaerial environment of Mars. As will be seen, the outcome of this evaluation helps explain additional, peculiarly Martian aeolian features (large longitudinal ripples, and transverse aeolian ridges) not found on Earth.

This paper begins by summarizing aspects of aeolian saltation and ripple development on Earth necessary for comparison with Mars (section 2). Next, the hypothesis that very large Martian ripples could be fluid drag bedforms, analogous to subaqueous bedforms on Earth, is evaluated in the context of previous laboratory work and observations from Mars (section 3). A second working hypothesis is proposed in which very large Martian ripples develop by saltation-driven impact splash, as aeolian bedforms generally do on Earth, but grow much larger on Mars due to lower prevailing wind dynamic pressures (section 4). Section 5 explains important implications and predictions of this second hypothesis. This second working hypothesis is found to be consistent with numerical experiments (section 6) and Mars rover observations (section 7). Section 8

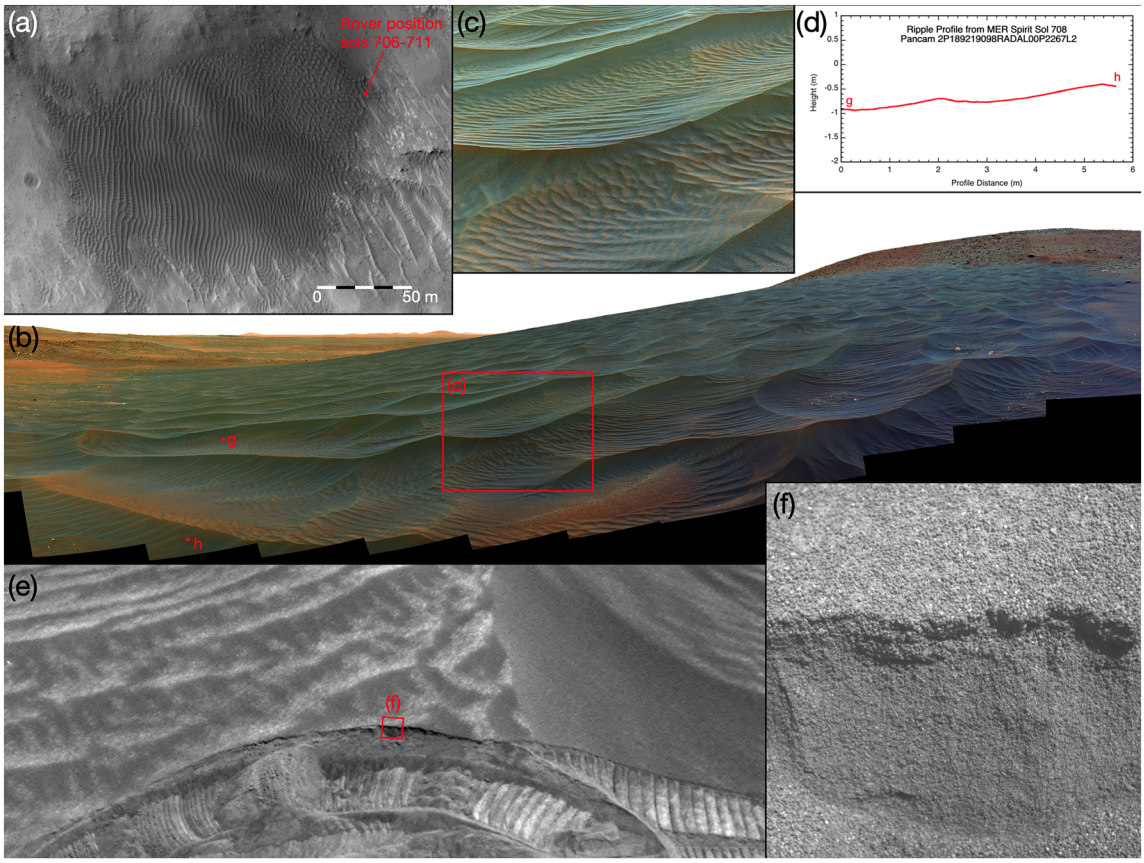

Figure 2. (a) El Dorado ripple field at Gusev crater, explored during Sols 706–711 of the MER *Spirit* mission. Relatively straight, continuous ripple crests prevail over the western and central portions of the ripple field. (Excerpted from HiRISE red filter PSP_001513_1655.) (b) False color view of the El Dorado ripple field obtained on Sols 708 and 710, spanning about 160° of azimuth. (Pancam sequences P2267 and P2268.) (c) Smaller secondary and tertiary ripples superimposed on the flanks of the largest, primary ripples. (d) Ripple profile between points "g" and "h" in panel (b) (from Figure 7 of Sullivan et al., 2008), confirms asymmetry apparent in panels (c), (b), (e) that is characteristic of dominantly transverse migration of primary crests. (e) Navcam (Maki et al., 2003) view of wheel scuff across crest of very large ripple. Red frame is location of Microscopic Imager (Herkenhoff et al., 2003) (MI) view in next figure pane. (Sol 711 Navcam image 2N189482856RADAL02P1950L0.) (f) MI view, 31 mm across, of "roadcut" near crest of very large ripple, showing rounded 200–300 μm grains at surface overlying a ~4 mm very weak crust, in turn overlying less sorted material at greater depths dominated by somewhat finer sand. (Sol 707 MI image 2M189124338RADAL00P2957.)

explains how this second hypothesis also helps to explain other, distinctively Martian aeolian bedforms such as large longitudinal ripples, and transverse aeolian ridges (TARs). Section 9 provides a summary, based on an overview diagram (Figure 21).

2. Comparing Aeolian Ripples on Earth and Mars

On Earth, aeolian ripples form in cohesionless sand when wind mobilizes grains into trajectories that bounce downwind, in a process known as saltation. Within a fully developed saltation cloud under steady wind conditions, atmospheric boundary layer momentum is transferred to saltating sand grains in flight, reducing wind strength near the surface to approximately $u_{*\mathrm{ti}}$, the impact threshold wind friction speed (e.g., Bagnold, 1941, pp. 31–33; Kok et al., 2012; Ungar & Haff, 1987), which is ~20% below the fluid threshold $u_{*\mathrm{tf}}$ required for initiating saltation by mobilizing grains directly by fluid drag (Bagnold, 1941, pp. 88, 94). (The fluid threshold $u_{*\mathrm{tf}}$ referred to here and throughout this paper is the minimum steady u_* required to initiate a sustained, saturated saltation cloud over a flat bed.) Consequently, grain movements from the bed within a saltation cloud in steady wind conditions are driven primarily by saltating grain impacts that "splash" other grains downwind during rebound, rather than by fluid drag mobilizing grains directly from the surface (e.g., Anderson, 1990; Bagnold, 1941, pp. 31–32; Kok et al., 2012; Martin & Kok, 2017). For

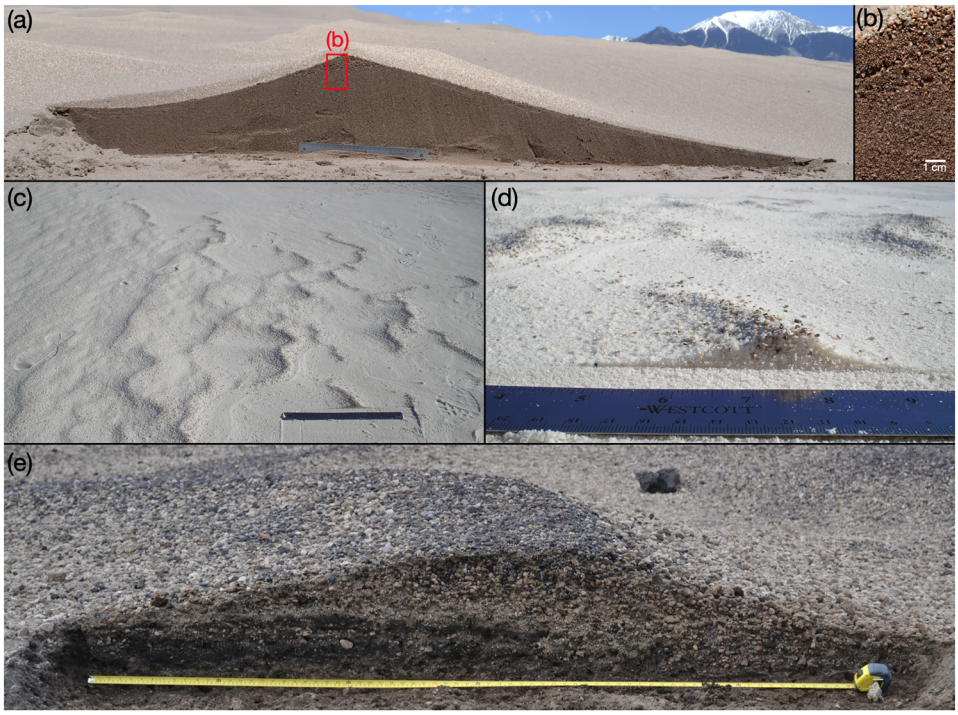

Figure 3. Diversity of bedforms developed in poorly sorted sands, in which the most massive, coarsest mobile grains can be driven only in creep-like motion by the impacts of saltating grains. Terminology for these features (megaripple, coarse-grained ripple, granule ripple, etc.) is inadequate (McKenna Neuman & Bédard, 2016), but the term "megaripple" is adopted throughout this paper for convenience. (a, b) Although crests are covered with very coarse, creep-only grains, bulk volumes of megaripples commonly are dominated by finer, saltating grains. (Great Sand Dunes, CO.) (c, d) "Megaripples" do not have to be large, as shown by this example with ~1 cm height and of ~14 cm cross-sectional span (White Sands, NM). (e) Coarse grains at crests can exceed granule (2–4 mm) size, as shown in this example from Askja, Iceland, in which crest grains are ~1 cm.

this reason, aeolian ripples are commonly referred to as "impact ripples" to distinguish them from subaqueous ripples, which form by a different mechanism.

Morphologies, sizes, and growth rates of terrestrial aeolian impact ripples are the essential basis for comparison with Mars. Grain sorting provides a useful organizational framework that will be utilized throughout this paper: (1) In well-sorted dune sand on Earth, small impact ripples form in minutes from a flat surface, eventually developing wavelengths on the order of ~10 cm and crest heights of several mm (e.g., Andreotti et al., 2006; Rasmussen et al., 2015; Sharp, 1963) (Figure 1). (2) Less-sorted sands permit the growth of larger ripples, where coarser grains concentrate along crests (e.g., Bagnold, 1941, p. 145; McKenna Neuman & Bédard, 2016; Seppälä & Lindé, 1978). In less-sorted sands, the saltating impacts of finer grains splash coarser grains downwind less efficiently. (3) In poorly-sorted sands, impacting finer grains can advance very coarse grains (typically >1 mm) in only creep-like movements, creating bedforms with very coarse, creep-limited grains covering crests; these endmember bedforms (in terms of sorting) have been referred to variously as "megaripples," "coarse-grained ripples," "granule ripples," and other equivalent terms. Unfortunately, none of these terms accurately describes the characteristics of these bedforms (which do not have to be enormous, are usually dominated volumetrically by their finer-grained interiors despite very coarse surface grains, and have coarse fractions that are not always granule-sized) (e.g., Bagnold, 1935, 1941, pp. 154–157; Fryberger et al., 1992; Greeley & Iversen, 1985, pp. 151–154; Jerolmack et al., 2006; Sharp, 1963) (Figure 3). Considering this diversity, we utilize the term "megaripple" throughout this paper in a simple, broad sense to refer to any impact ripple of any size that has a coarse fraction covering crests that moves only in creep (driven by impacts of finer saltating grains), thereby constraining bedform migration rate (e.g., Figure 3). Sharp (1963) suggested that >50% coverage of crests by creep-limited grains is required for megaripples to become well-developed, a standard we adopt here and apply to Martian features later in the paper. In this framework, megaripples are significant as endmember bedforms in terms of their (poor) material sorting.

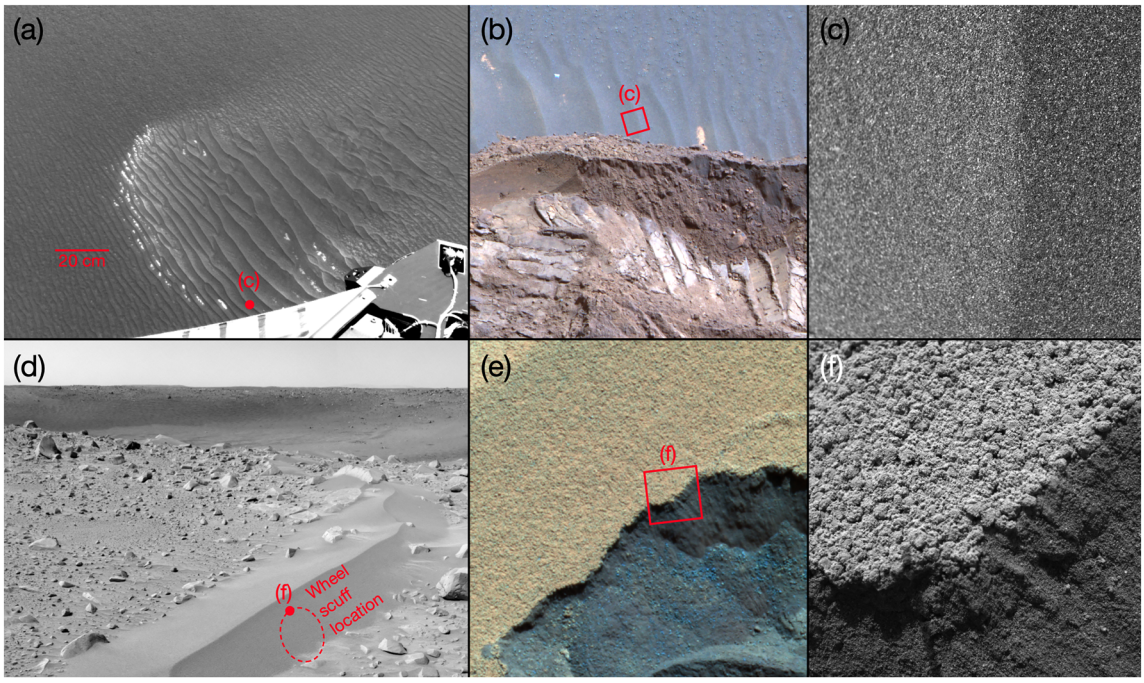

Figure 4. Examples of Martian bedforms similar to Earth at endmember grain sortings. (a–c) Well-sorted sands endmember: Small impact ripples of well-sorted ~100 μm sand on the floor of Eagle crater, Meridiani Planum. View (a), obtained while the rover was still on its lander base, shows the ripple area before wheel trenching there on Sol 54. Views (b) and (c) were obtained after the wheel trench. Microscopic Imager (MI, Herkenhoff et al. (2003)) view of (c) is 31 mm across. (Views (a)–(c) sources: Navcam Sol 005, P1541, 1N12862428RAD0205P1541L0; Pancam false-color Sol 055, sequence P2404; and MI 1M133070623CFD06GOP2956 from Sol 055, respectively.) (d–f) Poorly-sorted sands endmember: Megaripple at rim of Bonneville crater, within Gusev crater. Megaripple is ~14 cm high, with cross-sectional width of ~1.3 m, and was wheel-scuffed to reveal finer ~100 μm sand at depth overlain by dusty, rounded ~1 mm grains. MI view displayed in (f) is 31 mm across, same scale as (c), enabling direct comparison. (Views (d)–(f) sources: Navcam Sol 071, P1949; Pancam false-color Sol 073, P2557; and MI 2M132842058CFD2000P2977 from Sol 073, respectively.)

Additionally, the largest known megaripples (de Silva et al., 2013; Gillies et al., 2012) are endmembers also in terms of bedform size, representing the largest examples on the impact ripple size continuum on Earth (Ellwood et al., 1975; Lancaster, 2009; McKenna Neuman & Bédard, 2016; Wilson, 1972).

On Mars, rovers have encountered ripple morphologies with grain sorting characteristics familiar from Earth, ranging from small ≤10 cm wavelength ripples of well-sorted ~100 μm sand, to poorly sorted megaripples with surfaces of 1–2 mm grains overlying interiors of finer material (e.g., Arvidson, Anderson, Bartlett, Bell, Blaney, et al., 2004; Arvidson, Anderson, Bartlett, Bell, Christensen, et al., 2004; Arvidson et al., 2006, 2011; Greeley et al., 2004; Jerolmack et al., 2006; Soderblom et al., 2004; Sullivan et al., 2005, 2008; Weitz et al., 2006, 2018) (Figure 4). However, the Mars Exploration Rover (MER) mission encountered very large ripples of a type unknown on Earth. These enigmatic, enormous ripple bedforms have heights of ~20 cm, wavelengths of ~3 m, and surfaces that also host superimposed ripples of smaller, more conventional size (Figure 2). Despite overall dimensions comparable with large terrestrial megaripples, dominant grain size near crests was only 200–300 μm, similar to typical small impact ripples in dune sands on Earth. Because very coarse grains were absent, these Martian bedforms were not interpreted as megaripples, but as outsize (but otherwise ordinary) impact ripples (Sullivan et al., 2008). If this interpretation is correct, an important question was left unaddressed: How could impact ripples with such modest grain sizes grow so much larger on Mars than on Earth?

3. Are Very Large Martian Ripples Fluid/Wind Drag Bedforms?

Very large ripple morphologies similar to the MER examples also were encountered by the Mars Science Laboratory (MSL) rover (Figure 5) but were interpreted differently as fluid drag (specifically "wind drag") ripples in which wavelength λ is controlled by the same mechanism that controls λ in subaqueous current ripples on Earth (Lapotre et al., 2016; Lapotre & Rampe, 2018). Reasons for this interpretation include:

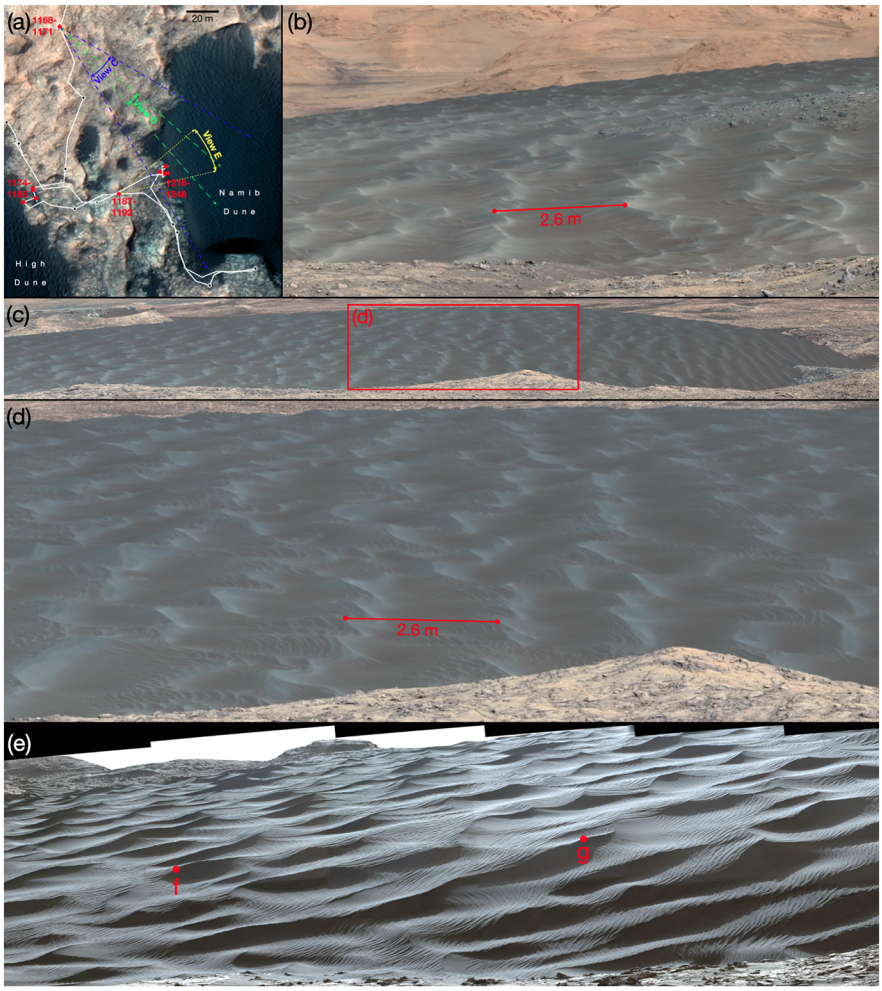

Figure 5. Examples of very large transverse ripples encountered along the MSL traverse during the Bagnold dunes campaign at Gale crater. (a) Overview map (HiRISE basemap imagery) showing MSL traverse in white between the margins of Namib dune and High dune, and the locations of views (c)–(e). (b) View toward the NW margin of High dune, aligned with well-developed transverse ripple crests that contrast with more reddish trough materials. (Color stretched excerpt from Sol 1,270 mcam05946.) (c–d) View aligned with well-developed transverse ripple crests on Namib dune, showing similar wavelengths and crest/trough color contrasts. (Color stretched excerpts from Sol 1,169 mcam05302.) (e) Sol 1,190 view of Namib dune margin where MSL rover stopped later, Sols 1,221–1,244. High phase angle of this observation conceals grain size-related color contrasts, but emphasizes surface morphology, revealing intricate secondary ripple patterns that in many places partially overprint each other. For scale, distance between points "f" and "g" spans ~7.4 m. (Sol 1,190 mcam05392).

(1) the atmosphere on Mars has a significantly higher kinematic viscosity than on Earth; (2) sinuous crest lines of Martian very large ripples are morphologically similar to subaqueous bedforms (this point was not included in Lapotre & Rampe, 2018); and (3) measurements of ripple wavelengths on Mars reveal a meter-scale mode distinct from smaller ripple wavelengths, implying two different controlling mechanisms: conventional impact splash for the smaller ripples, and fluid drag for the larger ripples (Lapotre et al., 2016). This section evaluates fluid/wind drag as a working hypothesis, assessing points (1–3). This hypothesis is relevant also to evaluating fluid drag bedforms more generally in a range of planetary conditions (e.g., Duran Vinent et al., 2019).

On Earth, the wavelength range of sand ripples forming under water in unidirectional currents overlaps with the wavelength range of aeolian impact ripples, despite very different fluid properties and sediment transport mechanisms (e.g., compare compilations of ripple wavelengths in Figures 8-3 and 8-6 of Allen (1982)). This fact forewarns of the challenge on Mars attempting to distinguish between formative ripple mechanisms primarily on the basis of wavelength. Evaluating a fluid drag hypothesis for large aeolian

Table 1
Comparison of Selected Sediment Mobility Parameters, Earth and Mars

Property	Earth subaqeous saltation H_2O (298°K)	Earth subaerial saltation, air (1 bar, 293°K)	Mars subaerial saltation, CO_2 (6.7 mb, 250°K)
Fluid dynamic viscosity μ (Pa s)	8.9E−4	1.8E−5	1.3E−5
Fluid density ρ_f (kg/m^3)	1,000	1.2	0.015
Fluid kinematic viscosity ν (m^2/s)	8.9E−7	1.4E−5	8.8E−4
Grain density ρ_g (kg/m^3)	2,650	2,650	3,000
Grain/fluid density ratio, ρ_g/ρ_f	2.7	2,200	200,000
Dominant mechanism for bed grain movement	direct fluid drag	impact splash	(impact splash)

ripples on Mars is complicated further by a smaller wavelength mode attributed to impact splash. Because the relative roles of impact splash and fluid drag are uncertain, two versions of the hypothesis are evaluated: fluid (wind) drag as the ripple forming mechanism; and fluid (wind) drag only controlling ripple wavelength λ.

In the first version of the fluid drag hypothesis, large aeolian ripples on Mars could be fluid drag ripples forming similarly to bedforms in gentle underwater currents on Earth. There are significant differences between saltation in air and saltation in water that are relevant for evaluating either process as a mechanism for aeolian ripple development on Mars. Two important factors controlling the differences between saltation in air and saltation in water are the density ratio between the grain and fluid, ρ_g/ρ_f, and large differences in dynamic viscosity, μ (Table 1) (e.g., Anderson & Anderson, 2010, pp. 463–464; Bagnold, 1941, pp. 72–75; Durán et al., 2012). On Earth, sand saltation in air involves relatively high ρ_g/ρ_f and low μ. This allows high-speed saltating grains to descend from the fastest part of their trajectories down through lower, slower portions of the atmospheric boundary layer without losing much speed, resulting in high-energy rebounding impacts that vigorously splash other grains, many of them downwind. The same is not true under water, where a sand grain descending toward the bed is slowed significantly by μ that is ~50 times greater than in air, and by momentum exchange all along the grain's path that involves fluid density much closer to grain density. As a result, sand grains saltating in water have relatively slow contact speeds with the bed, producing little or no impact grain splash (e.g., Schmeeckle et al., 2001). Consequently, subaqueous bedforms are not created by the cumulative effects of high-speed impacts vigorously splashing other grains, as in aeolian saltation. It is significant that on Mars, ρ_g/ρ_f is even higher than for aeolian saltation on Earth, by a factor of 90 (Table 1), indicating that impact splash should be at least as important on Mars. On this basis, terrestrial aeolian saltation involving high-speed impact splash is the appropriate analog for wind-driven grain movements that create bedforms on Mars, and ripples developed from saltation impact splash should predominate.

A second version of the fluid drag hypothesis for large Martian ripples would attribute sand transport primarily to saltation impact splash (as suggested by reasoning above, Table 1), but with ripple wavelength λ still controlled by the same fluid drag mechanism that controls λ for subaqueous fluid drag ripples. This hybrid concept is consistent with adoption of an impact threshold u_{*ti} for large ripple formative conditions by Lapotre et al. (2016), rather than a higher fluid drag threshold u_{*tf} that might otherwise relate to control by a fluid/wind drag mechanism. A relation describing how fluid drag controls ripple wavelength λ was proposed by Lapotre et al. (2017) and Lapotre and Rampe (2018)

$$\lambda \approx 2500 \frac{\upsilon^{2/3} D^{1/6}}{(Rg)^{1/6} u_*^{1/3}} \quad (1)$$

where kinematic viscosity $\nu = \mu/\rho_f$, D = grain diameter, $R = (\rho_g - \rho_f)/\rho_f$, and g = gravitational acceleration (about 3.71 m/s^2 on Mars). This relation, developed from a compilation of terrestrial subaqueous ripple data, is appropriate for flow conditions specified by $\chi < \sim 4$, where $\chi = Re_p \tau_*^{1/2}$, with $Re_p = (u_* D)/\nu$, and $\tau_* = u_*^2/(RgD)$. (This is an updated, dimensioned version of a similar, dimensionless approach presented in Lapotre et al. (2016)). Figure 6a applies Equation 1 to Martian conditions similar to large ripple settings at rover landing sites within Gusev crater and Gale crater. Warmest daytime conditions permit

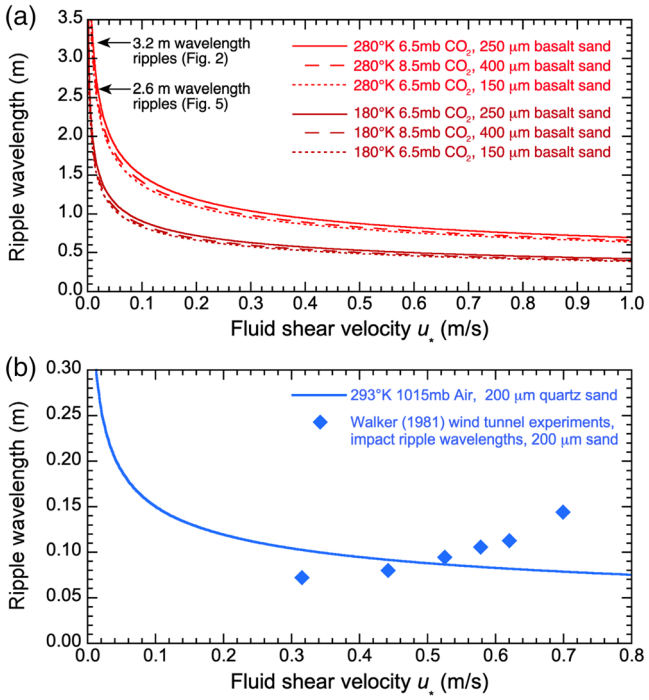

Figure 6. (a) Equation 1 applied to a range of Martian conditions (approximately representative of Gale and Gusev craters) predicts very low u_*, well below predicted u_{*ti}, for fluid/wind drag controlling ~3.2 m wavelength ripples at Gusev (Figure 2), ~2.6 m wavelength ripples on High dune and Namib dune at Gale (Figure 5), and similarly sized active ripples elsewhere on Mars. (b) Equation 1 compared with impact ripple wind tunnel experiments of Walker (1981) with 200 μm sand. Over a shared wavelength range, Walker's results (filled diamonds) differ systematically from Equation 1 due to impact splash as the formative mechanism. (Walker's experiment at $u_* = 0.315$ m/s yielding $\lambda = 0.072$ m has no counterpart in Equation 1 because $\chi \geq 4$ when $u_* > 0.8$ m/s.)

larger ripple wavelengths, but even so, Equation 1 predicts formative u_* only ~0.02 m/s or less for ~3.2 m wavelength ripples at El Dorado at Gusev crater (Figure 2), ~2.6 m wavelength ripples on High Dune and Namib Dune at Gale crater (Figure 5), and active ripples of similar and larger size in comparable settings elsewhere across Mars. We interpret formative $u_* \sim 0.02$ m/s to be improbably low (well below even modeled u_{*ti} for Mars, e.g., Kok, 2010a, 2010b), that would leave sand grains inert on the surface. (For example, $u_* < 0.02$ m/s corresponds to wind speed $u < 1$ m/s—equivalent in wind dynamic pressure to a gentle draft <0.2 m/s on Earth—at a height of 1 m for a wide range of Martian boundary layer configurations.) Adding to this problem is the relative inefficiency of fluid drag mobilizing grains on Mars compared with Earth. Atmospheric fluid drag in the Martian environment has been evaluated in previous laboratory experiments using Mars-appropriate kinematic viscosity $\nu = \mu/\rho_f$ (Greeley et al., 1980). Dynamic viscosity μ is slightly less for CO_2 than for air (e.g., Johnston & McCloskey, 1940; Laesecke & Muzny, 2017; Lemmon & Jacobsen, 2004), so kinematic viscosity ν is much higher for the Martian atmosphere only because ρ_f is ~80 times lower (varying diurnally and with elevation). Wind tunnel experiments at Martian kinematic viscosity ν (using CO_2 at low Martian pressure) with reduced-density sand grains to compensate for lower Martian gravity at grain first motion demonstrate that higher wind speeds are required on Mars than on Earth for fluid drag to mobilize sand (Greeley et al., 1980; Iversen & White, 1982; also cf. Swann et al., 2020 who did not use CO_2). To be clear, these experiments pertain only to first motions of grains as mobilized by fluid drag, not subsequent evolution of a mobilized bed into a saturated saltation cloud (in which saltation saturation length L_s is expected to be several times longer on Mars than on Earth (Pähtz et al., 2013)). As wind tunnel experiments, they could not simulate the full spectrum of time variable turbulence in a planetary-scale boundary layer (Pähtz et al., 2018), but serve well here for purposes of directly comparing aeolian fluid drag efficiency between Earth and Mars: Greeley et al. (1980) subjected the same suite of sediment test surfaces to turbulent boundary layers of both CO_2 and air, and at a range of chamber pressures from ambient down to 4 mb. Results showed that fluid drag mobilization of surface grains depends only on the boundary layer reaching a minimum wind dynamic pressure ($= \frac{1}{2}\ \rho_f\ u^2$) specific to each test surface, regardless of gas used or chamber pressure, with little influence from small differences in μ between CO_2 and air (Figures 1 and 2 of Greeley et al., 1980). The importance of wind dynamic pressure will be revisited in later sections.

Perhaps more important for purposes of this paper, a wavelength-based approach cannot distinguish between ripple formative mechanisms when their ripple wavelength ranges overlap. As an example, Figure 6b applies Equation 1 to a subset of terrestrial aeolian *impact ripple* wind tunnel experiments conducted by Walker (1981) with very well-sorted 200 μm sand (restricted to sieved 180–220 μm grains). If only utilizing Equation 1, the 0.08–0.14 m ripple wavelengths in Walker's experiments would appear consistent with fluid drag control similar to subaqueous current ripples. However, actual u_* values in Walker's experiments (filled diamonds in Figure 6b) show λ increasing with increasing u_*, as is typical of aeolian impact ripples (e.g., Andreotti et al., 2006; McKenna Neuman & Bédard, 2016; Schmerler et al., 2016). With due respect for the merits of Equation 1 to accurately describe wavelengths of subaqueous current ripples, such an approach cannot be used to distinguish between different ripple formative mechanisms with potentially overlapping wavelength ranges, especially in situations (such as Mars) where formative u_* is unknown. A multiple working hypotheses approach (Chamberlin, 1897), prompts a natural next question: Can conventional impact ripples grow large enough on Mars for wavelengths to overlap with the wavelength range proposed previously for fluid drag (Duran Vinent et al., 2019; Lapotre et al., 2016; Lapotre & Rampe, 2018)? Analysis presented in the following sections indicates the answer is yes.

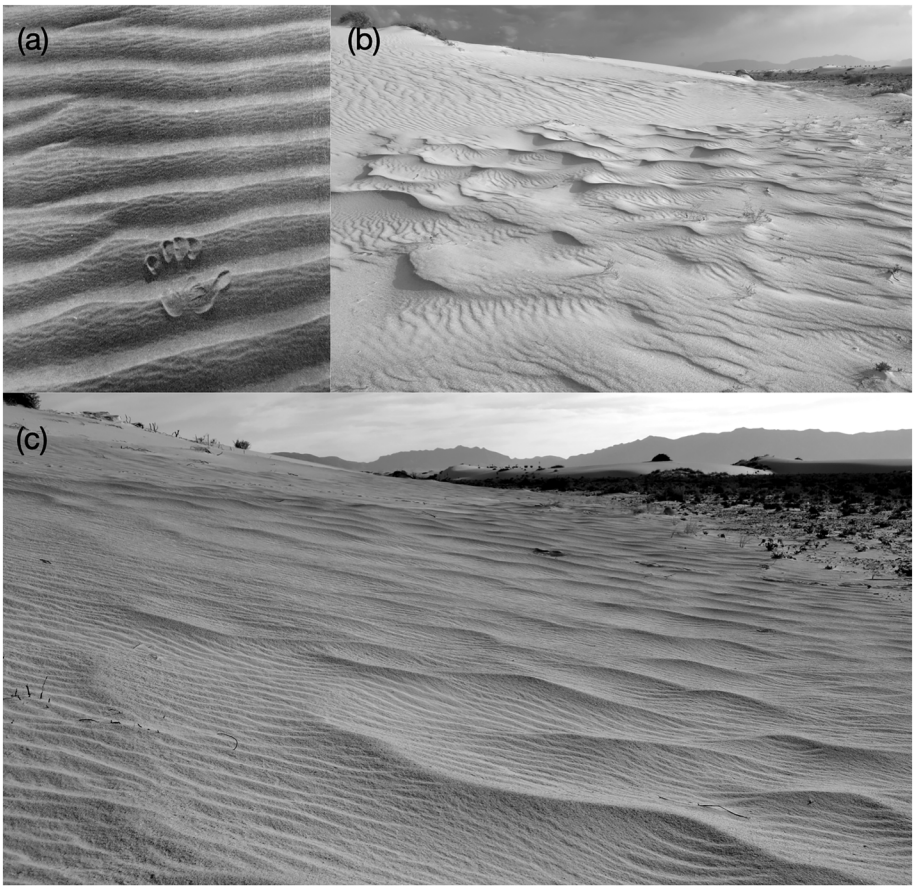

Figure 7. Terrestrial examples of impact ripples with multiple superimposed wavelengths. (a) Intermediate sorting case, excerpted from Figure 5 of Ellwood et al. (1975), from their study in the Algerian Sahara. (b, c) Poor sorting case (megaripples), both views at nearly the same location at White Sands, NM, USA, but 1 year apart.

Problems noted above explaining how wind drag might control the morphology of Martian large ripples motivate reconsideration of interpretations supporting this hypothesis (Points 2 and 3 in the opening paragraph of this section). Regarding Point (2), many examples of very large ripples on Mars actually have straight, instead of sinuous, crests. Some examples of straight-crested very large ripples are found at the Nili Patera dune field (Figure S3 of Bridges et al., 2012, supplementary material), at Gusev crater (Figure 2a), and at Gale crater (presented in section 7). Therefore, crest sinuosity or linearity cannot be diagnostic of origins. Regarding Point (3), conventional aeolian saltation on Earth can, by itself, produce multiple ripple wavelengths in the same setting, including smaller ripples superimposed on larger ones that all share the same orientation (Figure 7, detailed discussion in section 5.2; also Lorenz & Valdez, 2011, supplementary video). Multiple superimposed ripple wavelengths do not each require their own distinct formative mechanism, if the aeolian impact splash mechanism operates.

4. Are Very Large Martian Ripples Produced by Conventional Aeolian Impact Processes?

Ambiguities and other challenges applying fluid drag explanations to large Martian ripples motivate consideration of alternatives: On Mars, could the conventional impact splash mechanism somehow create much larger aeolian impact ripples than on Earth, with only 200–300 μm grains covering crests (e.g., Figure 2)? We approach this question by evaluating mechanisms that *limit* growth of aeolian impact ripples on Earth, but that might be less effective on Mars. Bagnold inferred from wind tunnel experiments that terrestrial impact ripple heights grow upward until wind dynamic pressure affects grain movements at crests (Bagnold, 1941, pp. 151–152). The precise mechanism(s) that might accomplish this are not fully understood and have received little attention, but could include: increased grain rolling and longer roll-out distances for

splashed grains, downwind extension of grain splash trajectories, and more pronounced turbulence effects at higher u_* affecting grains exposed more at crests than troughs (Appendix A). Numerical experiments accounting for some of these effects allow ripple heights eventually to stabilize with time (Manukyan & Prigozhin, 2009). Bagnold's concept is supported by ripple crests in well-sorted dune sands becoming flattened at higher wind speeds (higher wind dynamic pressures) (e.g., Bagnold, 1941, pp. 151; Sharp, 1963; Walker, 1981, pp. 142–145). Additional evidence supporting the idea that ripple growth is limited by wind dynamic pressure applying shear stress effects at ripple crests is provided also by the highest impact ripples on Earth (i.e., the largest megaripples), which have very coarse grains at crests that are more resistant against direct mobilization by greater wind dynamic pressures higher in the boundary layer.

Keeping in mind Bagnold's concept that wind dynamic pressure over growing ripple crests eventually limits ripple height, Martian surface conditions permit low saltation flux to be initiated by sporadic grain movements and sustained below u_{*tf} values required to initiate conventional higher-flux, saturated saltation clouds (Ewing et al., 2018; Sullivan & Kok, 2017; Swann et al., 2020), allowing impact ripples on Mars to migrate (albeit slowly and intermittently) entirely under prevailing conditions of relatively low wind speeds in the low-density Martian atmosphere. Importantly, these conditions represent relatively low wind dynamic pressures compared with Earth. These conditions should allow ripples on Mars to grow higher into the boundary layer before wind dynamic pressure effects would limit ripple growth. On Earth, wind dynamic pressures at moderate boundary layer $u_* > u_{*tf}$ limit ripple heights typically to <1 cm in well-sorted ~250 μm dune sand, and high boundary layer u_* values flatten and erase these ripples (e.g., Bagnold, 1941, pp. 151; Sharp, 1963; Walker, 1981, pp. 142–145). But on Mars, low-flux grain movements are driven by an atmosphere ~80 times less dense, at wind strengths prevailing below u_{*tf}, so the resulting low wind dynamic pressures should postpone interference with ripple growth until crests penetrate further upward into the boundary layer. We propose this effect contributes to allowing maximum impact ripple heights on Mars to be an order of magnitude higher than on Earth. The viability of this hypothesis is evaluated in the next three sections.

5. Effects of Wind Dynamic Pressure on Impact Ripple Development, Earth and Mars

5.1. Impact Ripple Initiation, Growth, and Size Control in Well-Sorted Sands

Bagnold's concept that wind dynamic pressure eventually limits impact ripple height has important implications that, when elaborated for the Martian environment, predict (1) a greater diversity of impact ripple sizes and relative ages on Mars compared with settings on Earth, and (2) that multiple, nested impact ripple sizes should develop in the same place sharing the same orientation, as has been observed. This section explains these two predictions, in preparation for comparisons later with numerical experiments and Mars observations.

We first briefly review essential background for these two issues. Previous work has revealed much about terrestrial impact ripple development that can inform the Martian case, but overall understanding of factors controlling maximum impact ripple size is incomplete. On Earth a flat, smooth bed of well-sorted dune sand exposed to saltation bombardment is quickly roughened by saltation impact pits (Bagnold, 1936). This flat but no longer smooth surface is unstable under continuing bombardment. Minor surface irregularities evolve rapidly into short, very small, immature ripples that migrate downwind at speeds inversely proportional to their individual sizes (e.g., Andreotti et al., 2006; Bagnold, 1936, 1941, pp. 146–147; McKenna Neuman & Bédard, 2016; Sharp, 1963; Walker, 1981). Average ripple size grows through consolidation, as smaller, faster incipient ripples catch up to and merge with slightly larger, slower features, making them even larger and slower (e.g., Anderson, 1990; Andreotti et al., 2006; Manukyan & Prigozhin, 2009; McKenna Neuman & Bédard, 2016; Prigozhin, 1999; Yizhaq et al., 2004). However, ripple consolidation and growth slow with time and then cease, resulting in fully mature ripples that migrate downwind with a stable, consistent wavelength (Andreotti et al., 2006; McKenna Neuman & Bédard, 2016; Walker, 1981). Although the rate of ripple consolidation should decrease with time as height disparity between remaining ripples narrows and average wavelength grows (Anderson, 1990), the factors leading to a stable, consistent height and wavelength are not fully understood.

Several studies examining this problem have sought to relate mature ripple wavelength to various grain trajectory length scales (e.g., Anderson & Bunas, 1993; Bagnold, 1941, pp. 149–151). However, mature ripple

wavelength is longer at greater u_* (until flattening occurs at extreme u_*) (Andreotti et al., 2006; Rasmussen et al., 2015; Schmerler et al., 2016; Walker, 1981, pp. 142–145), even though average grain trajectories within a saltation cloud vary with u_* only slightly (Creyssels et al., 2009; Ho et al., 2014; Namikas, 2003; Ungar & Haff, 1987). On this basis, additional or different factors besides grain trajectory length scales influence the ultimate, mature ripple wavelength (Andreotti et al., 2006; also reviewed by Durán et al., 2011; McKenna Neuman & Bédard, 2016). Complete closure of this problem is not the focus of this paper, but for purposes here we incorporate Bagnold's contribution of wind dynamic pressure limiting ripple height, by adopting the concept that ripples grow by consolidation as just described, until crests encounter sufficient wind dynamic pressure effects (see Appendix A for discussion) to arrest further growth upward (Manukyan & Prigozhin, 2009; cf. Katra et al., 2014). At this point all the ripples will be constrained to about the same maximum height, regulated by wind dynamic pressure effects at crests all along the bed. In this configuration the ripples have nearly identical size and therefore migrate at about the same speed, so it is difficult for any individual ripple to overtake another as the ripple train continues to migrate downwind. Any further adjustments in ripple wavelength (e.g., at *Y* junctions) occur under the constraint of a maximum ripple "height cap" enforced by various shear stress effects from prevailing wind dynamic pressure. On Mars in well-sorted dune sands, much lower wind dynamic pressures (very low ρ_f, and u_* generally below u_{*tf}) should allow ripple growth by consolidation to continue well beyond the stage where terrestrial wind dynamic pressures would arrest it, and this has two important ramifications discussed next.

5.2. Multiple Simultaneous Wavelengths of Impact Ripples on Earth and Mars

Low wind dynamic pressures on Mars are key to explaining why very large impact ripples have smaller secondary impact ripples migrating in the same downwind direction (resulting in more than one wavelength size mode, as noted by Lapotre et al., 2016) (Figures 2 and 5). On Earth as well as on Mars, this phenomenon derives from the incipient ripple formation process described above that involves the instability of a flat sandy bed under saltation bombardment. Specifically, formation of incipient secondary ripples between existing primary ripple crests on Earth or Mars should occur if two requirements are met: (1) the primary wavelength between established crests must have grown large enough, and surface area there must be long-lived enough (relative to ongoing migration of the previously established ripples) to allow impact pits there to evolve fully into recognizable secondary ripples; and (2) the surface grain size in such areas must be similar to the high-speed saltation flux. (If the target surface were coarser-grained than the high-speed saltation flux—as occurs in most extreme form at megaripple crests—impact splash pits cannot develop, preventing emergence of short, incipient ripples; cf. equation 1 of Anderson, 1987.)

On Earth in familiar settings of well-sorted dune sands, condition (1) is not satisfied because wind dynamic pressures arrest ripple growth too soon, before sufficient space has appeared for a second generation of recognizable ripples to develop, nested between the original closely spaced and relatively fast-moving crests which quickly overrun and obliterate the small trough surfaces in between. However, both conditions (1) and (2) can be satisfied on Earth at the other sorting extreme (megaripples). Megaripple crests, armored with very coarse grains, can penetrate higher into the boundary layer before being affected by wind dynamic pressures, and these higher crests are associated with greater bulk and therefore slower crest migration speeds, as well as longer wavelengths. (Ripple height and wavelength are linked in a complex fashion, not fully understood, with each influencing the other in different ways under different conditions; e.g., Andreotti et al., 2006. For purposes here, we note only that ripple height helps constrain the *minimum* possible wavelength associated with it, due to crests partly shielding trough floors from low-angle saltation; Sharp, 1963.) For megaripples, their slower migration speeds and longer wavelengths provide space and time for smaller secondary ripples to develop on their trough floors, as long as target sand there is similar to the high-speed saltation population so that impact pits can form (Figures 7b and 7c). Between the two extremes of sorting considered so far (well-sorted dune sand, and megaripples), Figure 7a presents an example of intermediate sorting where small secondary ripples have developed between primary crests (Ellwood et al., 1975; Wilson, 1972). To summarize the situation for Earth: secondary impact ripples nested between larger primary impact ripple crests will form in the poor sorting and intermediate sorting cases, but not in well-sorted dune sands.

On Mars, much lower wind dynamic pressures should allow impact ripples of all sortings—including sortings without an abundant coarser sand fraction—to penetrate upward into the boundary layer more easily and develop correspondingly longer wavelengths and slower migration speeds, satisfying conditions (1)

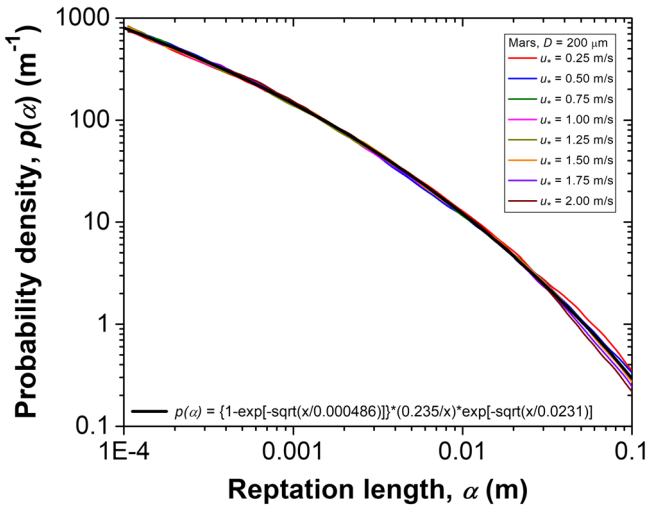

Figure 8. COMSALT simulations for the probability distribution of reptation lengths for transport of 200 μm particles at different shear velocities.

and (2) across the complete range of impact ripple grain size sortings. For these reasons smaller secondary ripples should be expected between crests of very large impact ripples on Mars. (In fact, we can think of no mechanism that could prevent this from occurring.) The line of reasoning presented here originates from the fundamental instability of a flat sandy bed under bombardment by high-speed, low-angle saltation, and assumes rather simply that this phenomenon exploits any exposed sandy area (on Earth or Mars) that satisfies requirements (1) and (2). Nothing in this line of reasoning restricts possible wavelength modes to just two; instead, multiple generations of nested impact ripples are possible, depending on planetary conditions, as long as they all collectively fit within the working space represented by the primary (largest) ripple wavelength. Finally, whether on Earth or on Mars, the nested nature of the secondary impact ripple process described here results unavoidably in statistical wavelength size "gaps" between the different nested ripple size populations. On Mars, development of multiple ripple wavelength modes is therefore an expected outcome from impact ripple dynamics known from Earth (Figure 7), but expressed over a wider range of sortings in the Martian environment specifically because prevailing wind dynamic pressures are much lower.

5.3. Implications of Longer Development Times for Larger Impact Ripples on Mars

On Mars, lower wind dynamic pressures allowing much larger maximum ripple sizes will be associated with longer ripple development times to reach full maturity. These extended development times enable a wide range of impact ripple sizes in various stages of development, potentially influenced by multiple formative wind directions, to be juxtaposed together in Martian aeolian settings. This contrasts with the familiar terrestrial experience of dune surfaces covered only with uniformly small, coherently oriented, mature ripples that quickly reorient to changes in wind azimuth, then migrate downwind unchanged in a mature state for as long as wind conditions persist (Figure 1). In Martian aeolian settings with limited sediment supply and/or subject to winds at multiple azimuths, we should be alert to the possibility that few, or none, of the bedforms available for inspection will have developed to the maximum ripple size that would otherwise be possible for their grain sorting.

6. Numerical Experiments of Large Impact Ripple Growth on Mars

If aeolian impact splash processes create very large ripples on Mars, then simply by virtue of their volumes, long time scales would be expected for impact ripples to reach their ultimate heights and sizes. This section describes numerical experiments that (1) estimate time scales for development of very large impact ripples on Mars, and (2) evaluate whether development of multiple, superimposed ripple wavelengths is a reasonable expectation during this process.

The experiments combined the COMSALT numerical model for saltation (Kok & Renno, 2009) with the numerical ripple development model of Yizhaq et al. (2004), a technique employed previously to evaluate small Martian ripples (11 cm wavelength) at Eagle crater on Mars (Yizhaq et al., 2014). The ripple model of Yizhaq et al. (2004, 2014) is based on a mathematical approach first developed by Anderson (1987). In this framework, a constant flux of saltating particles descends toward the bed at a low angle, and ripples develop from random, minor perturbations of a flat bed, according to how local bed slope variations control the local surface density of saltation impacts that drive the downwind flux of splashed grains (Anderson, 1987; Yizhaq et al., 2004). Details are provided in Appendix B, Kok and Renno (2009), and Yizhaq et al. (2004, 2014).

The model grid consisted of 4,096 points for a spatial dimension of 4 m (i.e., $\Delta x \approx 1$ mm) and a time step of 0.02 s. Wind velocity and direction (from left to right) are constant during the simulations. Experiments began with the bed having random, minor bed perturbations. Although ripples on Earth can form within minutes (e.g., Anderson, 1990; Andreotti et al., 2006; McKenna Neuman & Bédard, 2016; Rasmussen et al., 2015; Schmerler et al., 2016; Sharp, 1963), much lower Martian atmospheric density ρ_f results in a saltation impact rate that is about 2 orders of magnitude less on Mars (~10^6 m^{-2} s^{-1} for $u_* = 0.5$ m/s)

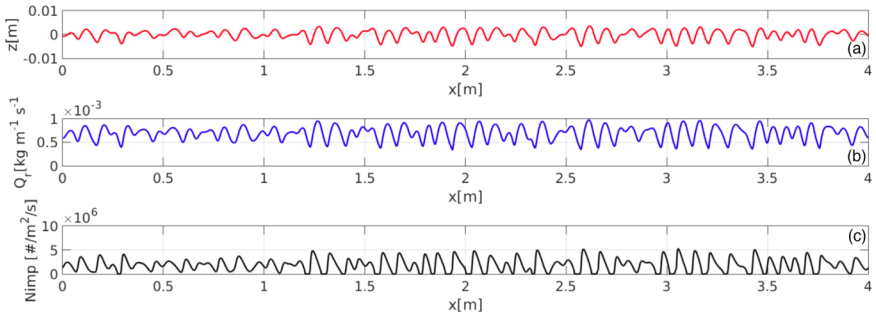

Figure 9. Ripples after 356 min of simulation for $u_* = 1.5$ m/s and $D = 200$ μm. Ripple heights (a) are still small. The reptation flux and the impact rate are shown in (b) and (c), respectively.

than on Earth (~10^8 m^{-2} s^{-1} for $u_* = 0.5$ m/s). For this reason alone, ripple formation should be much slower on Mars, independent of factors involving ultimate ripple size.

The ripple development model includes no provision for shear stress effects from wind dynamic pressure that would restrict ripple relief, so modeled ripples can continue to grow in height and/or wavelength. To make experiment durations more practical, relatively high $u_* = 1.5$ m/s was utilized to drive the saltation cloud because $p(\alpha)$ is independent of u_* (Figure 8), and cumulative reptation flux ultimately is what paces impact ripple evolution (Anderson, 1987, 1990). Because the numerical integrations are computationally demanding, we chose a 4 m-long grid and stopped the simulations before average ripple wavelength reached 1.5 m to avoid boundary influences.

Figure 9 shows ripple height, reptation flux, and impact density along the simulated bed after 356 min of experiment time. There are almost no saltation flux shadow zones at this early stage of ripple development. Figure 10 shows the same simulated ripple bed later, after 4,396 min of experiment time. At this stage maximum ripple heights are ~20 cm, similar to the very large ripples at Gusev crater in Figure 2. These results indicate that saltation impact splash alone—if unconstrained by effects of wind dynamic pressure—should allow very large impact ripples to develop under Martian conditions.

As previously mentioned, an important feature of Martian very large ripples is the presence of smaller ripples superimposed upon their surfaces, raising the question of whether two different formational processes are required. The numerical experiments here allow evaluation of whether impact splash reptation could, by itself, develop multiple ripple sizes, even with a monodisperse particle supply as in the experiments here. Many previous laboratory and numerical studies have documented how small impact ripples in their initial stages develop from very minor, randomized bed irregularities, such as those due to grain-scale bed roughness (e.g., Anderson, 1987, 1990; Andreotti et al., 2006; Bagnold, 1936, 1941, pp. 146–147; Durán et al., 2014; Manukyan & Prigozhin, 2009; Yizhaq et al., 2004, 2014). While this was the initial bed condition for seeding our numerical experiments, this type of small-scale roughness was not maintained during subsequent simulation time steps by continuously reapplying microscale roughness to the bed surface (as ripples emerged and

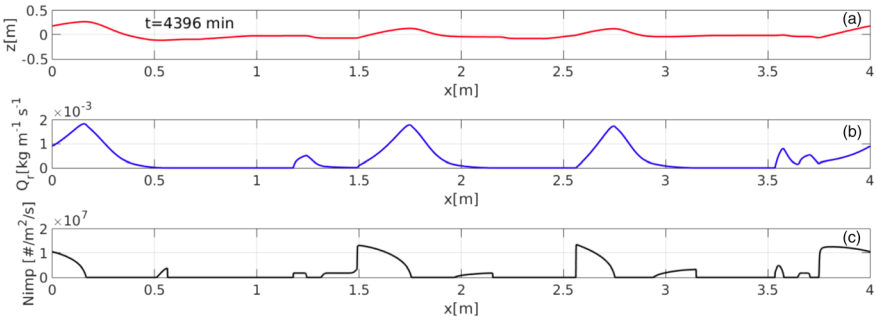

Figure 10. Ripples after 4,396 min of simulation for $u_* = 1.5$ m/s and $D = 200$ μm. The ripple height (a) is about 20 cm and the wavelength is 1.33 m. The reptation flux and the impact rate are shown in (b) and (c), respectively. Shadow zones are denoted by domains where the impact rate is zero and are located downwind of ripple crests.

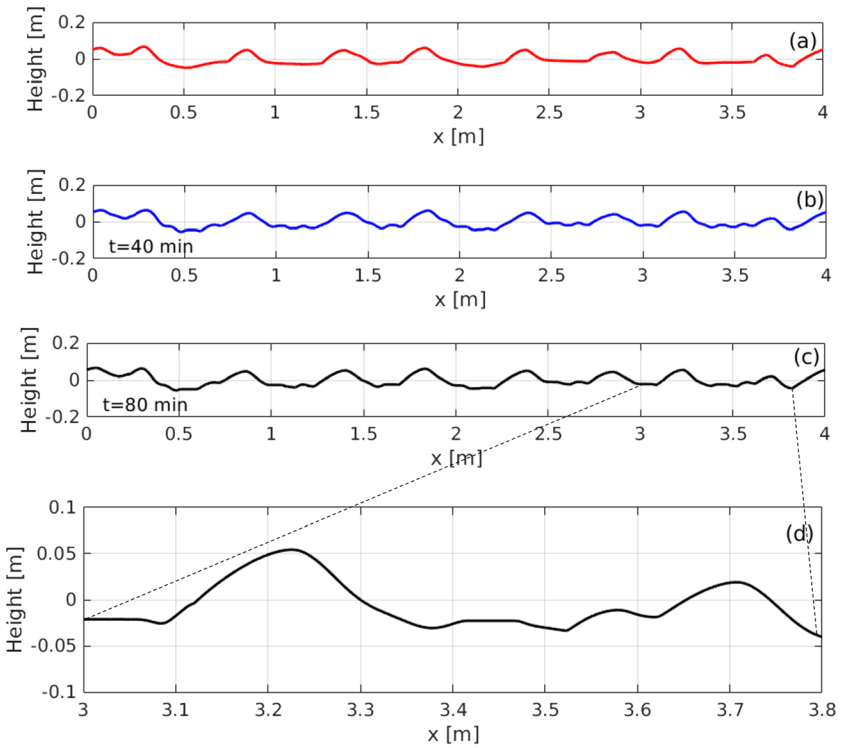

Figure 11. Application of the initial surface roughness condition to the ripple bed at 1,876 min, followed by 80 min of further saltation ($u_* = 1.5$ m/s, $D = 200$ μm, as before). (a) Ripple bed at 1,876 min, then (b) 40 min later, then (c) 80 min later. (d) Close-up of smaller ripples that developed in the troughs between the larger crests.

began coalescing to grow much larger than this initial roughness). In other words, the downwind migration of reptating material in the numerical model does not include creation of individual impact pits into the bed from high-speed saltation impacts. Instead, we reintroduced the starting roughness condition on to the rippled bed after 1,876 min, then allowed the simulation to continue as before for 80 min more. Results shown in Figure 11 indicate that among various new surface irregularities, small ripples developed in the larger troughs. (We examined why small ripples did not also develop on stoss sides of the preexisting major ripples. Stoss slope gradients are unconstrained in the simulations and become artificially steeper with increasing ripple size. These steep gradients result in intense saltation splash according to Equation B3, which causes rapid dispersion downwind of small ripples that encroach onto these surfaces.) These results indicate that development of very large ripples on Mars by impact splash should not, in the presence of ordinary grain-scale roughness, prevent the emergence of additional smaller impact ripples on surfaces between the larger crests.

For computational efficiency, the numerical ripple simulations involved relatively high boundary layer u_* applied constantly (i.e., no gusts) for the entire experiment duration. However, actual wind speeds on Mars are likely to supply much less energy to mobilize grains over equivalent time periods, based on climate model studies and limited in situ meteorological data (e.g., Anderson et al., 1999; Baker et al., 2018; Banfield et al., 2020; Fenton & Michaels, 2010; Fenton et al., 2005; Holstein-Rathlou et al., 2010; Lorenz, 1996; Murphy et al., 1990; Newman et al., 2017; Pla-Garcia et al., 2016; Spiga & Lewis, 2010; Sullivan et al., 2000; Viúdez-Moreiras et al., 2019a, 2019b). Approximate time scales of ripple development on Mars can be estimated crudely from the numerical experiments by using the relationship between time and ripple wavelength shown in Figure 12, and accounting for differences between reptation flux Q_r in the experiments and Q_r previously estimated from migration rates of Martian very large ripples observed from orbit. One of the highest estimated reptation fluxes for very large ripples on Mars we are aware of involves ripples migrating across dunes at Nili Patera, one of the most active aeolian sites on Mars. Bridges et al. (2012) derive a reptation flux Q_r of ~1.4 $m^3\ m^{-1}\ yr^{-1}$ for these ripples with average $\lambda = 4.6$ m migrating 0.03–0.27 m/yr (yr = Earth year). Transverse migration was assumed in their analysis, although later studies of very large

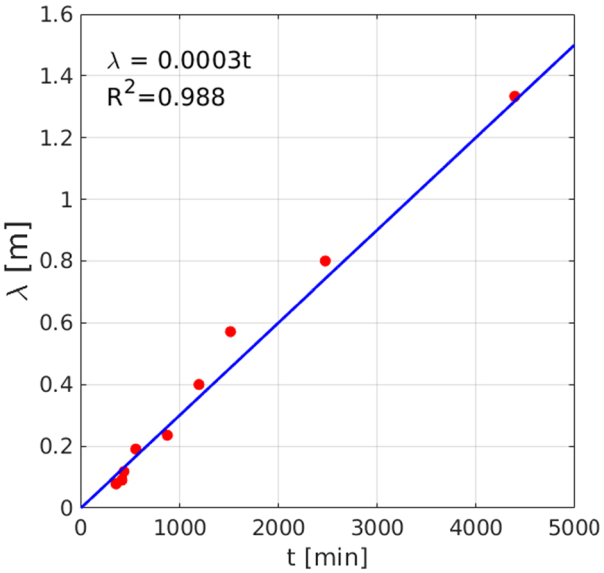

Figure 12. Development time t for ripple wavelength λ in the numerical experiments where $u_* = 1.5$ m/s and for $D = 200$ μm, with a linear fit.

ripple migration elsewhere on Mars have shown this assumption is not always reliable (Silvestro et al., 2016; Vaz et al., 2017). In the numerical ripple simulations, Q_r reached a maximum of 0.0018 kg/m/s over the largest ripple crests (=29 m^3 m^{-1} yr^{-1} using a bulk density of 1,950 kg/m^3), about 21 times higher than time-averaged Q_r reported for the Nili Patera ripples. A simplistic assumption of λ growing linearly with t (Figure 12) projects 15,200 min to develop $\lambda = 4.6$ m ripples in the same conditions as the numerical experiments. This equivalent experiment duration, combined with much lower Q_r for the Nili Patera ripples than in the numerical experiments, implies a minimum development time on Mars of ~220 days. (Of course, age is a different matter; these ripples could have been active for much longer if their current size represents full development that was achieved long ago.) Other, less active sites on Mars, where slower ripple migration rates have been reported, suggest even longer development times. For example, Silvestro et al. (2013) report ripples at Gale crater with average $\lambda = 2.7$ m migrating SW at 0.66 m/yr across the Bagnold dunes. Assuming a Ripple Index (RI = λ/h where h is trough-to-crest height) of 15 and applying the method specified in the supporting information of Bridges et al. (2012), $Q_r = 0.06$ m^3 m^{-1} yr^{-1}. The numerical experiment time to develop $\lambda = 2.7$ m ripples, from the relationship in Figure 12, would be 8,900 min, and accounting for the much lower Q_r at Gale than in the numerical experiments, the estimated minimum development time for the Bagnold ripples is ~8 years. (Silvestro et al. (2016) reported a group of smaller $\lambda = 1.9$ m ripples at Gale migrating faster, at 1.7 m/yr, but crest orientations were parallel to migration direction so the method of Bridges et al., 2012, which assumes transverse crest migration, cannot be applied.) The above time scale estimates incorporate several simplifying assumptions, therefore show principally only that development times for very large ripples on Mars are several orders of magnitude longer than for common impact ripples characteristic of well-sorted dune sands on Earth.

Differences on Mars between development times of the smallest and largest impact ripples under the same numerical experiment conditions help explain why aeolian settings on Mars commonly juxtapose multiple ripple sizes and orientations. Figure 12 indicates that common $\lambda \sim 10$ cm ripples can develop on Mars in a small fraction of the development time required for very large, meter-scale ripples. This allows many generations of small impact ripples to develop and/or reorient in areas between the very large impact ripple crests, without destroying their host bedforms.

7. MSL Rover Observations and Interpretations

7.1. Evaluating Ripple Origins With MSL Observations

The previous section utilized numerical experiments to evaluate impact ripple development at the low wind dynamic pressures of Mars. This section utilizes MSL rover observations to evaluate the fluid/wind drag and impact splash hypotheses, emphasizing the following: (1) rover observations elucidating how ripples with different wavelengths occur together in the same setting, to evaluate if a fluid/wind drag mechanism is required and to test predictions related to the impact splash hypothesis (sections 5.2 and 6); (2) rover observations of ripple height and grain size, to evaluate susceptibility of crests to aerodynamic effects (Appendix A), compared with very coarse-grained crests of comparably sized bedforms on Earth; and (3) an assessment of grain sorting, to place individual Martian bedforms into their appropriate context on the grain sorting continuum utilized in this paper for organizing discussion of bedform development on both Earth and Mars.

For assessing large ripple origins, we concentrate on ripples explored at the MSL Sol (Martian day) 1748–1751 site because data acquired there are particularly useful for testing the two working hypotheses. Very large ripples elsewhere were encountered by the MER rover at Gusev crater, and by the MSL rover while exploring the Bagnold dunes, but these encounters were limited in some important respects: (1) Although the MER encounter at Gusev crater had the advantage of the rover driving several meters directly into the ripple field (Figure 2a), the rover could not stay long to collect comprehensive data, because oncoming

winter compelled the solar-powered vehicle to move toward steeply sloping terrain elsewhere that would allow optimal orientation of the vehicle's solar panels to enable vehicle survival (Arvidson et al., 2008). (2) At Gale crater, the MSL rover encountered very large ripples several times while traversing between the Bagnold dunes (Bridges & Ehlmann, 2018; Chojnacki & Fenton, 2017; Lapotre & Rampe, 2018) but the Bagnold dunes were too hazardous to drive onto or across; instead, rover explorations were restricted to dune margins and small sandy patches in interdune areas (Figure 5a). Consequently, the MSL rover's arm-mounted instruments never reached crests of representative very large ripples on any of the main dunes (Appendix C).

Fortunately, very large ripples could be reached and inspected with rover arm-mounted instruments in more trafficable sand deposits later in the MSL mission. An example visited during Sols 1748–1751 is shown in Figure 13, a ripple field spanning approximately 85 m × 55 m with wavelengths up to 4.8 m. At this location a rover wheel track exposed the interior of a very large ripple, and representative crest and trough surfaces were directly reachable by the arm-mounted MArs Hand Lens Imager (MAHLI) camera (Edgett et al., 2012). This location also permitted close-range geomorphological observations from the mast-mounted stereo cameras (Navcam, and color Mastcam; Maki et al., 2012; Malin et al., 2017).

7.2. Ripple Grain Size Characteristics Correlated With Color Contrasts

Mature ripple size is highly dependent on grain size and sorting (e.g., Rasmussen et al., 2015; Sharp, 1963; Walker, 1981), so we begin with fundamental measurements of grain size. Hand-lens quality MAHLI images obtained at the MSL Sol 1,748–1751 location reveal differences in grain size and color between the crest and trough of the largest reachable ripple. In the ripple trough, reddish ~100 μm grains are common, mixed with coarser grains, whereas on the ripple crest the ~100 μm reddish grains are absent and ~400 μm grains are most abundant (Figure 13, cf. Weitz et al., 2018). This correlation between grain size and color, in which finer-grained trough materials are more reddish than coarser-grained crest materials, is consistent with MAHLI surveys of other large ripples in relatively dust-free sands along the MSL traverse (Ehlmann et al., 2017; Weitz et al., 2018, and supporting information therein). This correlation is expressed also in data from other MSL instruments such as Mastcam and ChemCam (Ehlmann et al., 2017; Johnson et al., 2017, 2018) (Figure 14). This correlation allows the extent of contrasting coarser versus finer dominant grain sizes to be identified across relatively dust-free bedform surfaces all along the MSL traverse, greatly extending more detailed grain size information from the spot locations where arm-mounted MAHLI images of aeolian bedforms have been obtained. Because we will utilize this correlation for multiple purposes, essential supporting details as well as limitations are discussed in Appendix D.

7.3. Testing Large Ripple Origins by Analysis of the MSL Sol 1,748–1,751 Ripple Field

A fluid/wind drag mechanism was invoked for the larger of two ripple wavelength size modes reported by Lapotre et al. (2016) and Lapotre and Rampe (2018). The impact splash hypothesis also predicts multiple ripple wavelength modes under Martian conditions, but the number of modes need not be just two. The relatively wide spacing between very large ripple crests in the MSL Sols 1,748–1,751 location provides room for an extensive display of superimposed impact ripples, in order to evaluate these two hypotheses in detail. Figure 15 diagrams a three-tiered system of nested ripple sizes. The largest ripples closest to the rover are ~30 cm high with λ ~ 4.3 m (Figure 13c). High-speed saltation trajectories on Mars are expected to descend mostly at low angles, as on Earth (e.g., Schmerler et al., 2016; Figure 13 of Sullivan & Kok, 2017), so the 30-cm-high ripple crest on the left of Figure 15 shields the lee slope and left portion of the main trough from most of the high-speed saltation flux passing left to right in this scene. As a result, saltation flux passing in this direction has greater effects on sand in the main trough starting a little less than halfway between the two largest ripple crests (black dashed line in Figure 15). From this position, small ripples emerge and grow progressively larger downwind, toward the very large ripple crest at the far right of Figure 15. As this train of secondary ripples increases in size, sufficient space begins to appear between secondary crests for a third "generation" of ripples to exploit and develop. This is consistent with the concepts of section 5.2.

A closer view provided by the mosaic in Figure 16 reveals grain size variations within this train of secondary and tertiary ripples. At the left end of the mosaic, small emerging ripples with λ ~ 3–4 cm are composed mostly of reddish, unresolved <150 μm grains, with coarser grains (perhaps subtending 2–3 pixels or ~400 μm) sparsely scattered across stoss slopes and more concentrated in lees immediately subjacent to

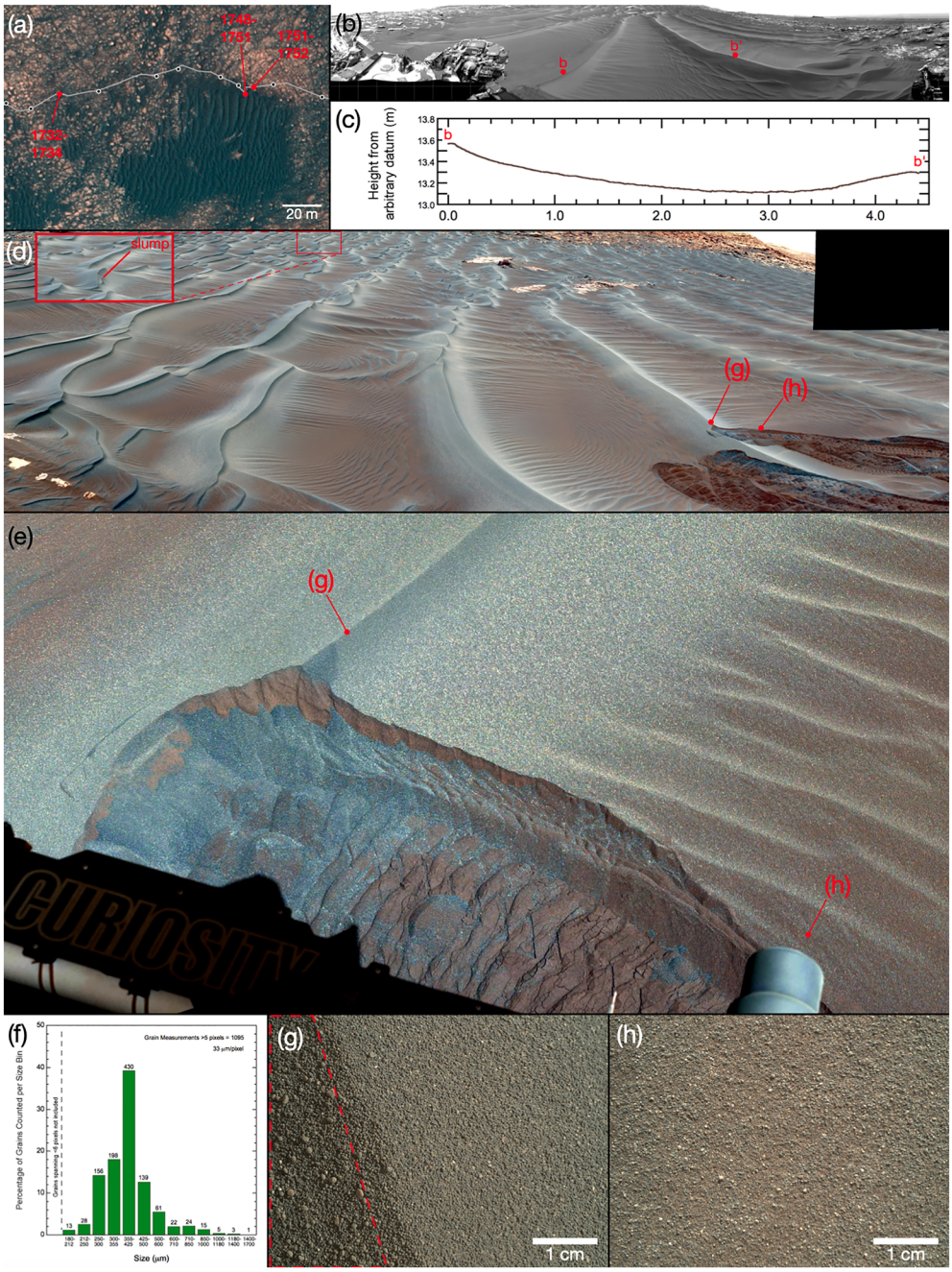

Figure 13. Very large ripples at Gale crater examined during Sols 1748–1751 of the MSL mission. (a) Overview HiRISE map showing part of the MSL rover traverse and the size and shape of the dark-sand ripple field. (b–c) Navcam mosaic spanning 330° of azimuth with location of 19-cm-wide topographic profile (b-b′) spanning 4.4 m between ripple crests. (Sol 1,748 Navcam ncam00255, ncam00354, ncam00376, ncam07553.) (d) General view of the ripple field, showing color contrasts between crests and more reddish troughs. Asymmetric profiles indicate formative winds left to right (approximately westward). Inset at upper left shows slump on lee face of large ripple; many other slumps are visible in images from the Sols 1,732–1,734 rover position (see view (a) for that rover location, and Sol 1,734 mcam09060 in archived material) which faces the lee slopes of this ripple field more directly. Locations of hand lens-scale MAHLI observations in views (g) and (h) are marked. (Sol 1,752 color-enhanced mcam09157.) (e) Part of the rover arm work area, showing locations of MAHLI observations of crest and trough materials in views (g) and (h) (which are 0.92 m apart). (Sol 1,748 mcam09139.) (f) Grain size-frequency at the crest, from 1,095 measurements of particles with diameters >5 pixels obtained from within the polygon marked by red dashed lines in the MAHLI image of view (g). Grains 250–500 μm are most common. (g, h) MAHLI views from 5.6 cm range of crest and trough materials (i.e., both views are at same scale for direct comparison, with scale bars 1 mm thick), showing very fine, reddish grains present in trough view are absent at crests, where ~400 μm grains are most common. Crest also has a scattering of much coarser grains >1 mm. Red dashed outline in (g) shows crest area of grain size-frequency measurements summarized in (f); count area avoided the steepest lee immediately subjacent to crest where coarser grains would preferentially roll away from. (Sol 1,749 MAHLI focus merged *z*-stacks 1751MH0007220000700516 and 1751MH0007220000700512).

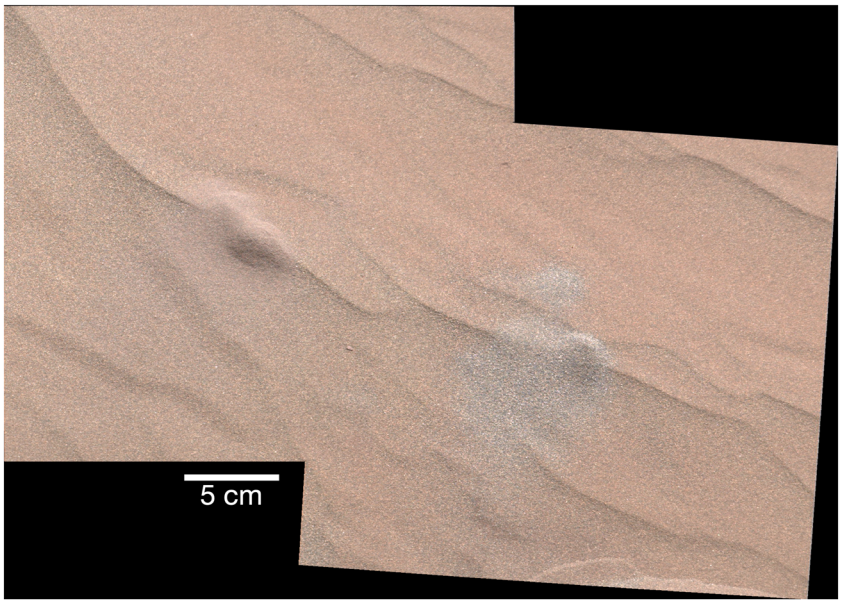

Figure 14. Mastcam mosaic showing color contrasts between grains sorted on board the MSL rover then later dumped into separate <150 μm (left) and >150 μm (right) piles, about 18 cm apart. (Sol 1,226 mcam05613 and mcam05614.) see also Figure 16 of Johnson et al. (2017).

crests (not at crests, as is common on Earth). As these secondary ripples get larger (middle of Figure 16a), coarser grains become scattered more abundantly over their surfaces. As spacing between secondary crests increases (even further to the right in the mosaic), small tertiary ripples dominated by <150 μm grains appear between the secondary crests, apparently exploiting this space in which to develop.

Migration speeds among this diversity of ripple sizes and surface textures will be faster for the smaller ripples, and slower for the larger ripples, implying that a somewhat hierarchical system of ripple sizes (with inversely related migration speeds) moves material across the main trough floor over to the bulk of the very large ripple at the right of Figures 15 and 16, which, because of its size, migrates most slowly of all. At the far right of Figures 15 and 16, secondary and tertiary ripples reaching steeper portions of the primary stoss slope degrade and disperse, probably for two reasons: (1) As discussed in section 6, low-angle saltation flux will become more concentrated on an impacting surface that is slightly back-tilted upwind, resulting in surface sand there being splashed downwind at a higher rate (e.g., Anderson, 1987, 1990; Bagnold, 1941, pp. 146–148;

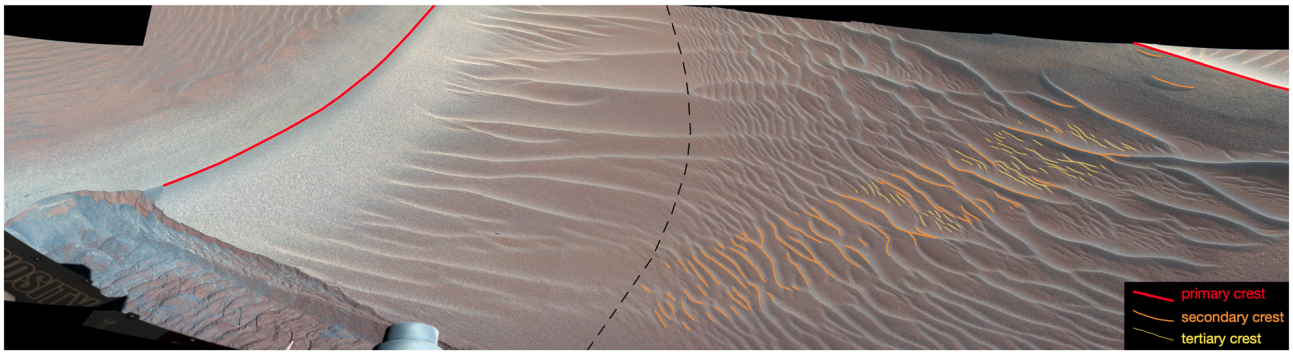

Figure 15. A three-tiered hierarchy of superimposed impact ripples is present at the MSL Sols 1,748–1,751 site. Primary ripple crests are marked in red. Primary ripples are large enough to shield the trough floor, left of the black dashed line, from low-angle, high-speed saltating grains passing left to right in this scene. Secondary ripples, marked in orange, begin to develop to the right of the shielded zone. As secondary ripples increase in size, progressing left to right, spacing increases sufficiently to allow development of a third "generation" of ripples to develop in between (marked in yellow). (Sol 1,748 mcam09139 and Sol 1,749 mcam09147.)

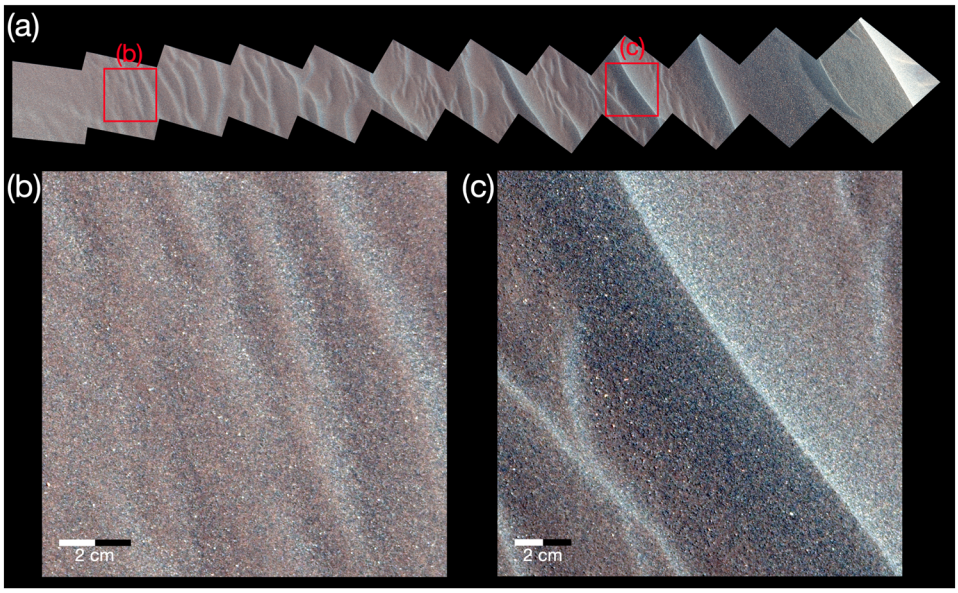

Figure 16. (a) Mastcam-100 coverage (Sol 1,749 mcam09145) provides a closer view of ripple changes across the center and right side of the main trough floor. This mosaic falls within the same area of the trough floor where primary, secondary, and tertiary ripple crests were identified in red, orange, and yellow in Figure 15. (b) Secondary ripples near the center of the trough have relatively low relief and are mostly unresolved <150 μm materials. (c) Further to the right (closer to the downwind primary ripple), secondary ripples have more relief and coarser surfaces.

Manukyan & Prigozhin, 2009; Prigozhin, 1999; Yizhaq et al., 2004; and many others; see also Equation B3 and Appendix A). This effect will cause a ripple migrating onto a steepening surface to spread its volume downwind, dispersing its height signature. (2) Coarser grains are more common closer to the primary (largest) ripple, and saltation impacts into this mixed grain size medium will splash any finer <150 μm grains present more vigorously downwind than >150 μm grains, accelerating dispersion of the finer fraction from secondary and tertiary ripples that reach and become exposed upon the steeper stoss flanks of the very large (primary) ripples.

Turning attention from stoss-related processes to lee slopes of the very large ripples, Figure 17 shows that individual coarse grains >150 μm moving over the brink collect on the lee slope, where high-speed saltation flux from the primary wind azimuth cannot easily reach (consistent with materials further downslope worked into secondary ripple orientations reflecting a different wind azimuth). These lee-side materials are therefore likely to be gradually overrun by the oncoming crest and become incorporated within it, then eventually reemerge and be reexposed on its stoss side (as the crest line passes on downwind), to be driven once more by saltation impact up the stoss toward the brink in a repeating cycle (Sharp, 1963; cf. Figure 3 of Anderson & Bunas, 1993). It is through these various saltation impact-related processes affecting stoss and lee slopes that very large ripples in Figures 13 and 15–17 seem to accumulate and retain their bulk as they migrate slowly downwind.

7.4. Grain Sorting: The MSL Sol 1,748–1,751 Ripple Field in Context

The MSL Sols 1,748–1,751 site at Gale crater allowed direct rover access to a field of very large ripples with wavelengths long enough to display key features for distinguishing among possible origins. Although these advantages can potentially inform our understanding of large ripples elsewhere at Gale and across the surface of Mars, it is important that these particular bedforms represent only one coordinate along a continuum in the framework of grain sorting, so grain sorting context must be established. Following the approach of Chamberlin (1897), we can evaluate whether the very large ripples in Figures 13 and 15–17 might be megaripples (as suggested by Lapotre and Rampe (2018) who applied to these bedforms the megaripple-equivalent term "coarse-grained ripples" from Jerolmack et al. (2006)). Dominant grain size at crests is only ~400 μm (Figure 13f) and for a megaripple interpretation this would have to be the creep-limited fraction.

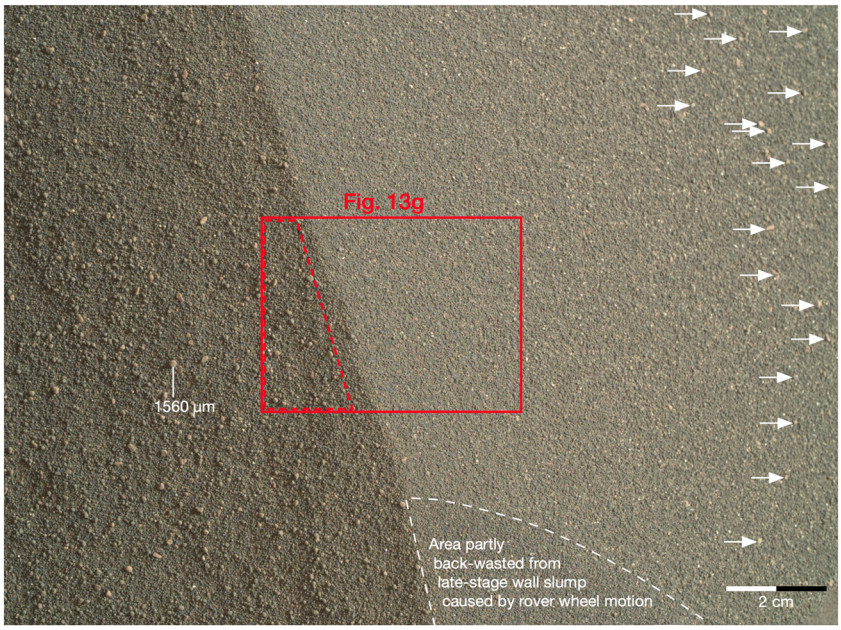

Figure 17. MAHLI 25 cm stand-off view of a primary ripple crest and subjacent lee obtained at the MSL Sols 1,748–1,751 position. This is a wider view of the same location shown in Figure 13g, the outlines of which are indicated by the red box (inside of which the dashed polygon indicates the area of grain size measurements reported in Figure 13f). Coarse grains as large as ~1,500 μm are scattered across the stoss slope and are not concentrated more closely together near the brink. Other examples (arrows) have rolled down the lee face and collected where slopes are less steep. (Sol 1,749 MAHLI 1749MH0007060010700437.)

However, an accessory population of much coarser grains up to ~1,500 μm is scattered widely across ripple surfaces (Figures 13g and 17), so it is these coarser grains that must instead represent the creep-limited size fraction. At the Sols 1,748–1,751 site, >1,000 μm creep-limited grains are too scarce to form congregations at crests (compare Figure 4f) that would constrain the migration rate of these bedforms, and they represent much less than a 50% covering of creep-limited grains indicated by Sharp (1963) as characteristic of well-developed megaripples. On this basis the large bedforms at the Sols 1,748–1,751 site are interpreted as very large ripples developed in sand not quite as well-sorted (~400 μm grains dominating crests) as the very large ripples at Gusev (200–300 μm grains at crests, Figure 2). Notably, the >1,000 μm grains sparsely scattered across the stoss are not congregated more closely together at the crest, indicating that active 30 cm-high ripples on Mars do not require armoring of crests by >1,000 μm grains against boundary-layer wind dynamic pressures, as would be expected on Earth (terrestrial megaripples).

Similar intermediate grain sorting characterizes sands of large ripples at two nearby locations, visited during Sols 1,181–1,185 (locations in Figure 5a), where crest/trough grain sorting (340–370 μm median crest grain sizes) is not much different from the Sols 1,748–1,751 bedforms, as displayed by crest-trough color contrasts and confirmed by MAHLI images (Ehlmann et al., 2017; Ewing et al., 2017; Weitz et al., 2018; Appendix D). Intermediate sorting similar to the Sols 1,748–1,751 ripple field probably also characterizes the extensive field of very large ripples on top of Namib dune, based on color contrasts there between crests and troughs indicating that crests are draped with grains dominantly >150 μm (Figures 5 and 14 and Appendix D). (Appendix C addresses a problem in a previously published claim, sourced from a feature misidentification at the Sols 1,221–1,244 rover location, that MAHLI images show no significant grain-size differences between small ripples and large ripples at Namib.)

8. Discussion

8.1. Wind Dynamic Pressure Effects Related to Other Martian Aeolian Phenomena

Previous sections have evaluated two working hypotheses to explain why transverse aeolian ripples grow very large on Mars. Numerical experiments (section 6) and rover observations (section 7) support saltation

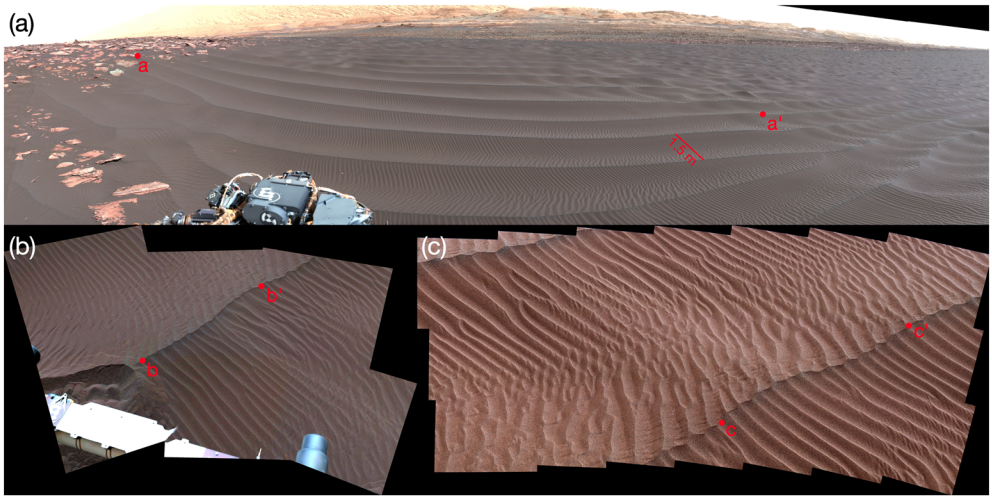

Figure 18. Longitudinal ripples viewed by MSL at the NE end of Nathan Bridges dune, Gale crater. (a) Formative SW winds, as determined from orbital analysis (Silvestro et al., 2016), blow left to right in this view that spans 146° of azimuth (making straight longitudinal ripples here appear curved). Longitudinal ripple extends about 20 m between points a-a′. (Color stretched Sol 1,601 mcam08154.) (b) Closer view nearer the rover, showing color contrasts consistent with surfaces dominated nearly everywhere by grains <150 μm, except small, weak concentrations of somewhat coarser, less mobile grains in small spots immediately subjacent to primary crests. Scale: b-b′ spans 1.0 m. (Color stretched Sol 1,601 mcam08150.) (c) Complex, intricate patterns of secondary and tertiary impact ripples superimposed on the primary ripples seem consistent with primary crests shielding different areas of trough surfaces from various low-angle saltation azimuths that are not perfectly aligned with trough axes. Scale: c-c′ spans 1.0 m. (Color stretched Sol 1,603 mcam08181.)

impact splash under conditions of low wind dynamic pressure as a formative mechanism. This same concept also helps explain other Martian aeolian phenomena: (1) large longitudinal ripples (section 8.2); and (2) TARs (section 8.3). These additional examples help illustrate how low wind dynamic pressures characteristic of boundary layer profiles on Mars, permitting a relatively lax "height cap" for maximum bedform size compared with Earth, enable greater diversity and complexity of Martian aeolian bedforms.

8.2. Low Wind Dynamic Pressures Enable Growth of Large Longitudinal Ripples

Longitudinal ripples on Mars are large enough to be recognized from orbit, their longitudinal nature revealed by long-term migration patterns that are consistent with sand transport primarily parallel with ripple crests, rather than transversely across them (Silvestro et al., 2016). Fields of longitudinal ripples were encountered by the MSL rover during the second phase of the Bagnold dunes campaign (Lapotre & Rampe, 2018). Figure 18 shows examples where crest heights commonly are <0.2 m and trough widths 1–2 m. Trough surfaces are covered everywhere with much smaller ripples having orientations consistent with sand migrating generally along the main trough axes, but these small ripple patterns are complex. Partially overprinted and interfering secondary and even tertiary ripple orientations are common along trough floor centers, and along upper flanks just beneath crests. The different orientations within these patterns are consistent with primary crests partially shielding selected areas of trough surfaces from low-angle saltation arriving from azimuths that are not perfectly aligned with trough axes (Figure 18). Figure 18 includes examples of longitudinal ripples extending over 20 m from behind small rock obstructions. Away from these obstructions, patterns of small ripples covering the main troughs imply that alternating wind azimuths not exactly aligned with the main troughs contribute to incremental back-and-forth shifting of primary crest positions. Color properties of sands in Figure 18 indicate grains >150 μm are relatively scarce at this location, and become weakly concentrated only in narrow zones immediately subjacent to primary crests. These zones probably function temporarily as oblique lees (from either side) whenever winds are not perfectly aligned down trough axes.

Terrestrial analogs for these large, longitudinal ripples are unknown to us. Some similarities are shared with terrestrial "sand shadows" of various types (Bagnold, 1941, pp. 189–191; Hesp, 1981; Hesp & Smyth, 2017; Yang et al., 2019; Zhao et al., 2019), in which a sand deposit extends downwind from a small, nonerodible

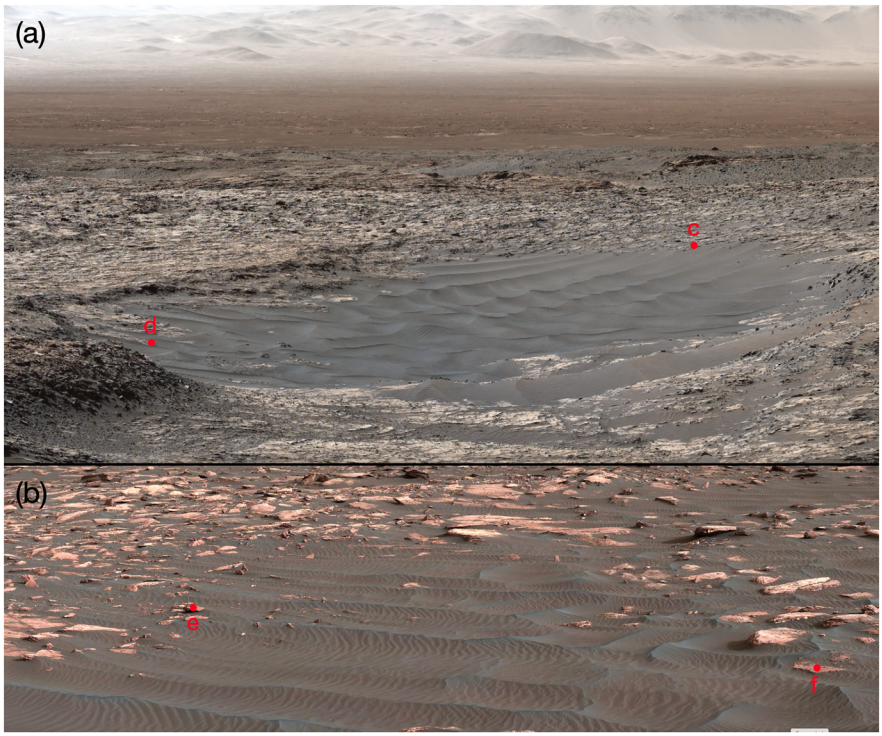

Figure 19. Two examples from Gale crater of longitudinal ripples transforming downwind into transverse ripples. (a) Sol 1,248 view across the floor of Gale crater capturing a 20 m × 10 m sand patch. Longitudinal ripples near point "c" transform into transverse ripples of comparable relief in the presumed downwind direction (approximately SW) toward point "d" 20 m away (mcam05827). (b) Smaller, lower longitudinal ripples migrating left to right, transforming into transverse ripples. Distance between points "e" and "f" spans 7.4 m. (Color-stretched Sol 1,628 mcam08415.)

obstruction (commonly a clump of vegetation, or an isolated rock) in a unidirectional wind regime. The sand deposit is stable only within the aerodynamic protection provided by the upwind obstruction, and shrinks downwind to its termination for two reasons: (1) small, natural variation of wind azimuths around the dominant wind direction create a triangular protection zone that narrows downwind behind the obstacle; and (2) even without small variations of wind azimuth, the boundary layer eventually recovers to normal strength downwind of the obstacle, as demonstrated even in the perfectly unidirectional flows of numerical and wind tunnel experiments (Hesp & Smyth, 2017; Yang et al., 2019). On Mars, where boundary layer wind dynamic pressures are much lower, neither of these effects should interfere with sand deposits extending far downwind from rocky obstructions, as long as overall relief of the longitudinal sand deposit does not exceed the effective "height cap" imposed by wind dynamic pressure effects appropriate for grain sorting, ρ_f, and u_* (the same factors enabling greater maximum relief of large transverse impact ripples than on Earth, as discussed earlier). An illustration of this principle is that rather than terminating downwind, Martian longitudinal ripples in many cases transform into chains of large transverse ripples (or complex longitudinal/transverse hybrids) of equivalent relief (Figure 19). These examples help illustrate the general diversity and potential complexity of interacting aeolian ripple sizes and morphologies that are enabled on Mars specifically by relatively low wind dynamic pressures of the boundary layer, which manifest as a less restrictive "height cap" for bedform development, diversity, and interaction than is possible on Earth.

Not all longitudinal ripples can be directly associated with individual rocky obstructions at what would seem to be their upwind ends, so not all longitudinal ripples originate in this way. Other possibilities might include a field of transverse very large ripples which become converted in place to longitudinal ripple behavior if wind azimuths change, or if a secondary wind azimuth more aligned with crests than transverse to them becomes more influential than previously. Whichever way a Martian longitudinal ripple becomes established, the bedform represents a substantial volume of sand capable of integrating the effects of multiple and varied wind events in complex ways over a long developmental history. For example, it might be

possible that an occasional wind event mostly transverse to longitudinal ripple crests could cause temporary transverse migration, or create deformities in places along the length of a longitudinal ripple. In such instances, when longitudinal sand migration resumes, presumably any "snub" upwind ends or deformities would migrate downwind along the longitudinal axis, perhaps at a rate roughly comparable to that of a transverse ripple of equal relief moving in the same direction.

These concepts evoke long-term orbital studies that have revealed complex migration patterns of large Martian ripples (Silvestro et al., 2016; Vaz et al., 2017). The migration patterns observed from orbit clearly differ from simpler behaviors of much smaller impact ripples on Earth (where small transverse impact ripples covering dune surfaces reorient quickly and coherently to changes in wind azimuth). These differences have raised uncertainties about whether Martian ripples large enough to be resolved from orbit form by the impact splash mechanism familiar from Earth (Silvestro et al., 2016; Vaz et al., 2017). In addressing this uncertainty here, the potential for impact ripples to grow much larger on Mars (sections 4–7) is pertinent, because much of the character of the complex, long-term migration patterns of very large Martian ripples observed from orbit (whether primarily transverse or longitudinal) is attributable simply to their greater bulk: The larger a ripple grows, on any planet by any mechanism, the more its bulk becomes too ponderous for complete reorientation to occur with each change of wind azimuth. The relatively high wind dynamic pressures on Earth allow only megaripples (i.e., impact ripples having crests armored with coarse, creep-only grains) to grow large enough to show similarly sluggish behavior. (In this vein, terrestrial megaripples have been described as behaving like "reptation dunes," Lämmel et al., 2018, although to avoid confusion, megaripples are true ripples because coarse grains concentrate at their crests, generally the opposite of dunes, Bagnold, 1935). On Mars, small impact ripples commonly are found partially overprinting each other with multiple orientations in settings exposed to multiple wind azimuths, indicating that even small impact ripples on Mars are subject to relatively slow reorientation (compared with Earth) due to low sand flux driven by winds generally below $u_{*\mathrm{tf}}$ (e.g., Figures 14 and 15 of Sullivan and Kok (2017)). Very long development time scales of much larger impact ripples (section 6) will make very large ripples proportionally even less responsive to changes in wind azimuth, so that very large impact ripples on Mars, whether primarily transverse or longitudinal, or functioning as hybrids in a complex wind regime, should not be expected to completely reorient to frequent changes in wind azimuth. Instead, their bulk will integrate the effects of multiple formative wind directions (including the effects of more transient, more responsive smaller ripples) in potentially complex ways, consistent with aspects of a "dune-like dynamic" observed from orbit (Silvestro et al., 2016).

8.3. Low Wind Dynamic Pressures Enable Growth of TARs

TARs are one of the most abundant aeolian feature types observed from orbit (Balme et al., 2008; Berman et al., 2011; Bourke et al., 2003; Malin & Edgett, 2001; Wilson & Zimbelman, 2004; Zimbelman, 2010) (Figure 20). TARs are light-toned, ripple-like bedforms, or perhaps small dunes, with heights up to several meters (e.g., Balme et al., 2008; Geissler & Wilgus, 2017; Hugenholtz et al., 2017; Zimbelman, 2010). A diversity of concepts to explain TARs has been proposed (e.g., Geissler, 2014; Zimbelman, 2010; Zimbelman & Scheidt, 2014) but origins remain unknown. A leading hypothesis is that TARs are analogous to terrestrial megaripples (e.g., Foroutan & Zimbelman, 2016; Hugenholtz & Barchyn, 2017; Hugenholtz et al., 2017). However, TARs in many instances are several times larger than even the largest megaripples known on Earth (e.g., Balme et al., 2008; Foroutan & Zimbelman, 2016; Hugenholtz & Barchyn, 2017; Hugenholtz et al., 2017).

Independent of any potential genetic relation between megaripples and TARs, we can consider whether different maximum megaripple sizes might be expected between Earth and Mars due to differences in prevailing wind dynamic pressures. For megaripples on Earth, a surface armor of very coarse grains allows crests to penetrate upward into the terrestrial boundary layer to heights of a decimeter or more. This armor is effective because it is invulnerable against direct mobilization by wind dynamic pressure effects during bedform growth and migration in normal formative winds, in which coarse grains undergo only short creep movements driven primarily by impacts from finer saltating grains. Megaripple height reduction or flattening can occur only during rare, uncommonly strong and extended wind events that are able to mobilize coarse grains into saltation either by direct fluid drag, or by intense impact splash from just the highest-speed fraction of saltating grains (that move in trajectories above most other grains of the saltation cloud, thereby extracting extra momentum from the boundary layer during extreme wind events) (Isenberg et al., 2011;

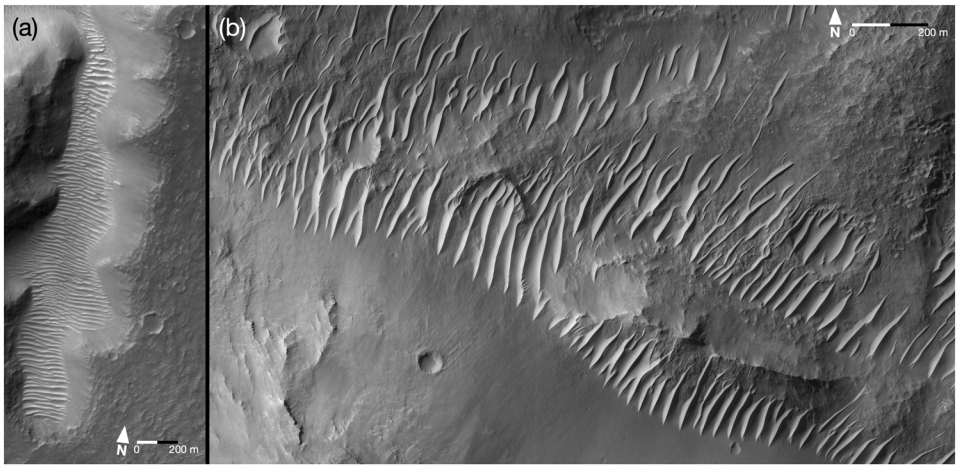

Figure 20. Examples of transverse aeolian ridges (TARs), one of the most abundant aeolian feature types observed from orbit. (a) TARs forming a continuous deposit on the floor of Nirgal Vallis. (Excerpted from MOC image E02–02651.) (b) A field of TARs with many individual bedforms not connected with each other. (Excerpted from HiRISE PSP_001684_1410_RED, original image centered Lat. −38.864°, E Lon. 196.019°.)

Katra et al., 2014; Yizhaq & Katra, 2015; Yizhaq et al., 2012). In such rare, extreme wind events, erosion of megaripple crests by the highest-speed saltating fraction becomes more likely when boundary layer $u_* \geq u_{*\mathrm{ti}}$ of the very coarse grains, and flattening is possible when $u_* \geq u_{*\mathrm{tf}}$ of these grains (Katra et al., 2014).

On Mars, megaripples with crests covered by 1–2 mm grains are common (Arvidson, Anderson, Bartlett, Bell, Blaney, et al., 2004; Arvidson, Anderson, Bartlett, Bell, Christensen, et al., 2004; Arvidson et al., 2011; Greeley et al., 2004; Jerolmack et al., 2006; Soderblom et al., 2004; Sullivan et al., 2005, 2008; Weitz et al., 2006, 2018). For 1 mm grains on Mars, numerical experiments predict $u_{*\mathrm{ti}}$ ~ 1–2 m/s, depending on modeling approaches and assumptions (Claudin & Andreotti, 2006; Kok, 2010a, 2010b; Kok et al., 2012; Pähtz et al., 2012), and $u_{*\mathrm{tf}} > 2$ m/s, modeled from wind tunnel fluid threshold experiments (Iversen & White, 1982; Swann et al., 2020). These are relatively high values, compared with prevailing wind strengths recorded by surface landers and rovers (e.g., Banfield et al., 2020; Holstein-Rathlou et al., 2010; Lorenz, 1996; Murphy et al., 1990; Sullivan et al., 2000; Viúdez-Moreiras et al., 2019a, 2019b), and predictions from numerical climate models (e.g., Anderson et al., 1999; Baker et al., 2018; Fenton & Michaels, 2010; Fenton et al., 2005; Newman et al., 2017; Spiga & Lewis, 2010). Nevertheless, predicted $u_{*\mathrm{ti}}$ and $u_{*\mathrm{tf}}$ values for 1 mm grains on Mars provide only crude estimates for boundary layer wind strengths that would limit megaripple growth or erase these bedforms, because they do not account for, among other things, how time-averaged shear stress $\tau = \rho_\mathrm{f} u_*^2$ of the atmospheric boundary layer relates to locally higher τ focused at exposed ripple crests as a function of their height (cf. Isenberg et al., 2011; cf. Siminovich et al., 2019).

An alternative approach that captures at least some of this effect involves comparing overall boundary layer conditions known to have flattened megaripples on Earth, to boundary layer conditions on Mars that would lead potentially to a similar outcome. Isenberg et al. (2011) report that small, 7-cm-high megaripples at Nahal Kasuy, Israel covered with 780 μm crest grains were erased by storm winds reaching 15 m/s at 3.3 m, corresponding to $u_* = 0.8$ m/s using their derived value of aerodynamic roughness for the rippled ground. Wind tunnel experiments involving flat beds of a wide range of tested grain sizes and densities indicate that boundary layer $u_{*\mathrm{tf}}$ must be ~3–7 times higher on Mars than on Earth to achieve the same effectiveness of first-motion grain mobilization (accounting also for lower Martian gravity), depending on similitude approach (Iversen & White, 1982; Swann et al., 2020). Applying a conservative ratio of 3 (from the approach of Swann et al., 2020), flattening megaripples on Mars identical to the Nahal Kasuy bedforms would require overall boundary layer u_* ~ 2.45 m/s, a friction speed well-exceeding in situ measurements by landers and rovers as well as predictions by numerical climate models. On the basis of these comparisons, despite their uncertainties, lower wind dynamic pressures of Martian boundary layers would seem to provide much less impediment to continued megaripple growth than on Earth. Lower wind dynamic pressures on Mars enabling megaripples to grow larger than on Earth provides an evolutionary path linking megaripples,

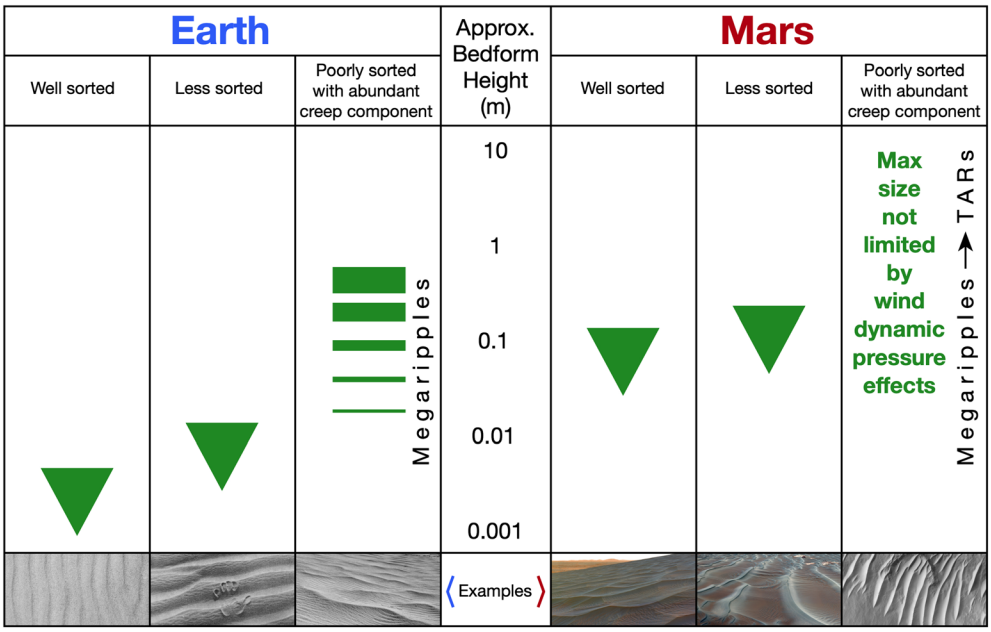

Figure 21. Summary comparison between Earth and Mars of wind dynamic pressure effects influencing maximum sizes of aeolian impact ripples as a function of grain sorting. For most grain-sorting cases, wind dynamic pressure effects become influential near the maximum bedform height, symbolized by inverted triangles within the columns. However, with increasingly poor sorting toward the megaripples case, wind dynamic pressure effects on Earth become less continuously regulatory and more stochastic and potentially destructive (see text for details), symbolized by the array of horizontal bars. On Mars, modeling based on wind tunnel experiments suggests much lower wind dynamic pressures there are less likely to cause similar destructive events to megaripples, allowing higher growth into the size range of TARs.

such as those investigated so far by rovers, to the origins of larger TARs seen abundantly from orbit across the Martian surface. On this basis, many TARs are likely to be megaripples that have grown very large, unhindered by relatively low wind dynamic pressures that prevail on Mars.

9. Summary of Wind Dynamic Pressure Effects on Bedform Size, Earth and Mars

Throughout this paper the parameter of grain sorting to help frame comparisons between terrestrial and Martian ripples. (In ranging from one extreme of relatively fine, well-sorted dune sands, through intermediate sortings, to the poorly sorted materials of megaripples at the other extreme, for simplicity we have ignored the specific and rare case of well-sorted but universally coarse materials.) Figure 21 uses grain sorting as a framework to summarize, in a simplified way, how differences in wind dynamic pressure between Earth and Mars contribute to different bedform morphologies on the two planets, and how lower wind dynamic pressures on Mars enable a greater diversity of impact ripple bedform morphologies there. In most instances the effects of height-limiting wind dynamic pressure become influential only near the maximum bedform height for a given grain sorting, so in Figure 21 this is symbolized informally by triangles widening upward within columns as bedforms approach typical maximum sizes.

For example, in well-sorted dune sands on Earth (leftmost column of Figure 21), incipient impact ripples emerge rapidly from an initially flat bed and grow in height and wavelength through consolidation. During this initial phase, wind dynamic pressure sweeping across the surface is too small to curtail development of the initial, very low surface relief. But as the ripples continue to consolidate and grow upward into higher speed regions of the boundary layer, the effects of horizontal wind dynamic pressures begin to limit further height growth, expressed informally in Figure 21 by the triangle in the leftmost column widening with increasing bedform height, reaching maximum influence at a representative limiting ripple height of several mm (typical of well-sorted dune sands, e.g., Andreotti et al., 2006; Sharp, 1963; Walker, 1981). Even after an approximate mature ripple height has been reached for grain size and prevailing boundary

layer conditions, ripple wavelength might continue to evolve slowly, but with height still modulated by wind dynamic pressure effects. This is a dynamic equilibrium in which the potential for continued ripple growth is continuously contending against the effects of wind dynamic pressure imposing uniform ripple height (therefore also uniform migration speed), with the ripples themselves providing some mutual aerodynamic protection of each other to allow growth upward to reach maximum crest height for grain size at crests and prevailing wind conditions. Intermediate grain sortings, with somewhat coarser grains available to protect crests from stresses imposed by the boundary layer, are portrayed in Figure 21 as capable of somewhat greater maximum ripple heights. Toward the poor-sorting endmember case (i.e., megaripples, the third column of Figure 21), the influence of wind dynamic pressure on ripple height becomes less continuously regulatory in character and, instead, increasingly stochastic and potentially maladroit. This is because megaripples have crests armored with very coarse grains that are relatively impervious to direct mobilization by wind, so megaripples are capable of continuing to grow in height (and thus wavelength), until rare, exceptionally strong wind events move even the coarsest grains into saltation. These events can result in destruction of the bedform rather than height regulation of it (Isenberg et al., 2011; Katra et al., 2014; Yizhaq & Katra, 2015; Yizhaq et al., 2012). This is portrayed in Figure 21 informally by an array of horizontal bars becoming more prominent (approximately: more likely) with bedform height. On Mars, similarly destructive, size-limiting mechanisms do not seem available to curb megaripple height, due to very low available wind dynamic pressures combined with very coarse grains at crests. This is reflected in Figure 21 by poorly sorted materials on Mars being capable of evolving from megaripples of the smallest sizes all the way to TARs that in some instances have bedform heights near 10 m (e.g., supplementary material associated with Shockey & Zimbleman, 2013). Because wind dynamic pressure would seem to have little influence curbing the growth of megaripples on Mars, these bedforms likely are limited in size by other factors, such as local history of sediment supply that, when interrupted, might also include long periods of inactivity leading to induration.

Figure 21 summarizes that on Earth, coarsening of crest grains is required to allow impact ripple crests to penetrate upward into the boundary layer more than several mm. On Mars, maximum ripple height increasing with crest grain size seems apparent in the few examples directly encountered so far by rovers (large ripples ~20 cm high with 200–300 μm crest grains at Gusev, ripples ~30 cm high with ~400 μm grains dominating crests in less sorted sands at Gale) but only if these examples indeed represent fully mature bedforms having achieved maximum heights for their respective crest grain sizes under similar formative u_*. Future rover missions could test and improve this relationship by additional encounters with fully-mature, very large ripples, closely inspecting grain sorting at crests.

10. Conclusions

Planetary exploration is undertaken for many reasons, including opportunities to test the potential universality of an evolving body of knowledge in environments different from Earth. On Mars, very large aeolian ripples such as those in Figures 2, 5, and 13 represent this type of opportunity. MER and MSL observations show these bedforms have crests covered with only modest grain sizes rather than creep-limited grains, so they are not megaripples. These bedforms might form by the same saltation impact splash mechanism of much smaller ripples on terrestrial dune surfaces—but if so, an explanation is needed for why Martian conditions should enable larger sizes. Alternatively, these large Martian ripples have been interpreted previously as fluid/wind drag bedforms with wavelengths controlled in a manner similar to subaqueous current ripples on Earth.

Theoretical models of hydrodynamic/aerodynamic drag ripples understandably include simplifications, e.g. ripple wavelength serving as a proxy for overall ripple size (assuming constant λ/h, or Ripple Index, RI), and/or uniformly-sized grains within bedforms. Unfortunately, neither of these assumptions adapts well to evaluating an impact ripple working hypothesis. As discussed in Appendix A, RI values commonly vary 10–25 for aeolian impact ripples on Earth, including megaripples. Ripples with RI > 25 (flatter ripple shapes) occur in well-sorted dune sands and/or at higher formative u_* (e.g., Bagnold, 1937, 1941, pp. 151–152; Sharp, 1963; Walker, 1981, pp. 142–145). Bagnold reported RI of 30–70 while working with well-sorted dune sands and, knowing that some grain size variation still exists even in the most well-sorted natural sands, wondered how impact ripples might form, if at all, in a hypothetical sand composed only of truly identically-sized grains

(Bagnold, 1937, p. 431). On Earth, high RI ripples forming in well-sorted sands at high u_*, compared with lower RI ripples forming in less sorted sands and/or at lower u_*, indicate the influence of the following: (1) grain size *contrast*, even within a unimodal sand supply; (2) the associated differential susceptibility this contrast represents to wind dynamic pressure effects as coarser grains start concentrating at crests; and (3) fluctuating wind dynamic pressures of the boundary layer. In this concept, planetary boundary layer conditions combined with grain sorting are able to regulate impact ripple height more directly than wavelength. Wind dynamic pressure increases with height most rapidly closest to the surface, and this would seem to represent more direct leverage for the boundary layer to influence ripple heights than wavelengths. Beautifully repeating wavelength patterns of small impact ripples covering dune surfaces have attracted attention for generations but, perhaps less noticeably, consistent heights within these same ripples seem to be as remarkable and important, but have received less attention for detailed explanation (Appendix A). Control of mature ripple height by boundary layer wind dynamic pressure effects interacting with grain sorting in turn helps constrain minimum ripple wavelength (Sharp, 1963).

Ripple wavelengths can be easier to measure and compare than ripple heights (e.g., Sharp, 1963). But for purposes of this paper, a limitation of a wavelength-only perspective is that it cannot distinguish between different ripple formative mechanisms when their wavelength ranges might overlap (e.g., Figure 6b). A multiple working hypotheses approach prompts the question: On Mars, can impact ripples grow large enough for their wavelengths to overlap with those proposed for fluid/wind drag? The answer is yes, when lower wind dynamic pressures of Martian boundary layers are accounted for (sections 4 and 5), and as indicated by numerical experiments (section 6). Numerical experiment results support the hypothesis that Martian ripples of all observed sizes can develop by the impact splash mechanism. The numerical experiments included no provision for wind dynamic pressure effects that would limit ripple relief as on Earth, so the numerically modeled ripples continued to grow through consolidation, suggesting how saltation impact splash could develop larger impact ripples on Mars. Numerical results also showed that smaller impact ripples emerge spontaneously on surfaces between larger impact ripples (Figure 11), accounting for the coexistence of multiple ripple sizes.

On Earth, impact ripples are ubiquitous in aeolian settings worldwide, for reasons explained in section 2. Aeolian ripples potentially of fluid/wind drag origin are rarely reported and such interpretations are equivocal (e.g., the singular wind tunnel experiment of Bagnold, 1941, pp. 165–166; Wilson, 1972). Prime reasons why impact splash is the dominant subaerial ripple-forming mechanism on Earth are relatively low μ, and high grain/fluid density ratio $\rho_g/\rho_f \sim 2{,}100$ (section 3; Table 1). Nevertheless, fluid drag is an essential component of the impact ripple process. Fluid drag initiates aeolian saltation on both Earth and Mars by mobilizing a fraction of surface grains (e.g., Pähtz et al., 2018; Williams et al., 1994), and should increase splashed grain roll-out distances at crests (Manukyan & Prigozhin, 2009). Even in a saturated saltation cloud, where average u_* at the surface is lowered below fluid threshold, fluid drag must still affect the flights of any grains in motion. The conclusion offered in this work is that very large ripples on Mars are impact ripples that have developed in the same way as on Earth—incorporating similar contributing roles played by fluid drag—rather than being fundamentally different fluid/wind drag bedforms as proposed in previous work. On Mars, mature impact ripples are larger only because the same mechanisms regulating mature impact ripple heights on Earth are delayed to greater heights (and thus, indirectly, longer wavelengths) because wind dynamic pressures are lower in the Martian boundary layer.

Aeolian settings on Mars that display multiple wavelength size modes (i.e., with statistical size "gaps" in between) should be expected when all ripples form by the impact splash mechanism (section 5.3). This is notable because previous work has cited evidence of two wavelength size modes as requiring two different formative mechanisms (impact splash for the smaller mode, fluid/wind drag for the larger mode (Lapotre et al., 2016; Lapotre & Rampe, 2018)). On Earth, saltation impact splash is known to produce multiple wavelength modes in settings with poor grain sorting (e.g., Figures 7b and 7c), and in settings with intermediate grain sorting (e.g., Figure 7a), but not in well-sorted sands because these materials are most susceptible to wind dynamic pressure effects that halt ripple growth too soon (trough surfaces between ripple crests are too short, are quickly overrun by relatively fast-moving crests). Mars thus seems to represent a more universal case, where much lower wind dynamic pressure should allow impact ripples of all sortings to penetrate upward into the boundary layer more easily, with correspondingly longer wavelengths and larger overall

sizes that permit secondary ripples to form between primary crests. In this process, secondary ripples naturally cannot fill-out the full continuum of wavelengths up to and including their primary hosts. The smaller (therefore faster) secondary ripples developing between crests of their much larger (therefore slower) hosting primary ripples simply do not have the downwind fetch to develop all the way to the same size as their hosting primaries.

Impact ripple growth to much larger sizes on Mars requires longer ripple development times, during which wind azimuth is expected to vary even in settings where a single wind azimuth is most common. In these settings, transverse impact ripples that reflect the dominant wind direction should gradually grow larger with time, but at any given moment should also display small, more reactive and thus more transient ripples superimposed at orientations reflecting only the most recent saltation wind azimuth. This helps explain juxtapositions of a diversity of interacting ripple sizes of different relative ages and orientations in many Martian aeolian settings (e.g., Figures 2, 5, 13, and 15), where many of the bedforms would not be at maximum possible size for their grain sorting and prevailing u_*. (This differs from dune surfaces on Earth covered by uniformly small, coherently-oriented, mature ripples that quickly and completely reorient to changes in wind azimuth.) In these settings the smallest impact ripples that have developed most recently, potentially from any wind direction, should be abundant as a first mode in a wavelength size-frequency histogram. Larger impact ripples, developed primarily by many wind events from the most formative, recurring wind direction, will take much longer to reach full-sized maturity, but when conditions permit this, these bedforms will cease growth after reaching their maximum "end state" size, so that long-term evolution should lead to an accumulating ripple size population also in that part of a wavelength histogram to gradually reinforce a second, larger wavelength size mode. The multiple superimposed ripple sizes and orientations apparent in Mars rover images do not require multiple formative mechanisms; all that seems to be required is plenty of sand, aeolian saltation under conditions of relatively low wind dynamic pressure (allowing larger maximum ripple sizes, so an enormous span of relative ages), and time.

MER and MSL rover observations reported here support the hypothesis that conventional saltation impact splash operating under low wind dynamic pressures enables a more extended size range of transverse ripples on Mars than on Earth. As expected from this hypothesis, rover observations indicate that ripple crests 20 cm high covered with 200–300 μm grains (El Dorado ripple field at Gusev crater), or 30 cm high covered with ~400 μm grains (MSL Sols 1,748–1,751 position), do not require armoring by much coarser grains, as do lower-relief megaripple crests on Earth against the effects of greater wind dynamic pressures in terrestrial boundary layers. Rover observations also reveal that where wavelength spacing between the largest ripple crests is unusually great, even a three-fold hierarchy of nested impact ripple sizes can develop, consistent with an impact splash mechanism. Explanations offered here for larger transverse impact ripples on Mars also help explain other Martian aeolian bedform types unknown on Earth. Low wind dynamic pressures on Mars should impose a less restrictive "height cap" on bedform development for any type of grain sorting, allowing a diversity of bedforms to develop to larger sizes on Mars (Figure 21). Examples discussed in this work include large longitudinal ripples and megaripples capable of growing to the size of TARs. In conclusion, the saltation impact splash mechanism known from Earth, but operating in the lower wind dynamic pressures of Martian boundary layers, helps to explain the greater size range, and diversity, of aeolian bedform morphologies found on Mars.

Appendix A: Ripple height-limiting mechanisms and wind dynamic pressure

A grain saltating downwind along a cohesionless, sandy surface loses momentum at every rebound through grain splash and other deformational effects applied to the bed (e.g., Rice et al., 1995). The grain continues saltating only if its momentum can be recharged during flight through exchange with the boundary layer. Most high-speed saltating grains, which move rapidly downwind as they rebound along the bed, have effectively no residence time on any particular ripple, but provide energy to grains on the bed that comprise such bedforms. Following Bagnold (1941), pp. 146–148 and many others, we focus on grains splashed relatively short distances for discussing how impact ripples grow and develop their ultimate shapes and sizes. Starting with the simplest case of a level bed under low-angle bombardment from high-speed saltating grains, a small sample surface patch will experience no net deposition or erosion if grains are splashed from upwind into the surface patch at the same rate as they are splashed out of it downwind (the rate of grain

arrivals equals the rate of grain departures). Bagnold modeled the initiation of ripples by noting that on a bed with slight irregularities, any small surface patch with even a slight upwind tilt will experience a greater rate of high-speed saltation impacts per surface area, causing grains to be splashed out of it at a higher rate, resulting in net erosion. A similar patch tilted slightly downwind will experience fewer high-speed saltation impacts per area, causing fewer grains to be splashed out of it than are splashed into it, resulting in net deposition. In this way, incipient ripples develop stoss and lee sides as sites of net erosion and net deposition, respectively, that migrate downwind as a moving ripple with an approximately triangular cross section. Bagnold noted that wind speed very close to the surface must increase with height more rapidly over ripple crests than over troughs, and inferred that ripple height grows upward until the increased wind dynamic pressure across crests (relative to troughs) becomes sufficient to lengthen splash trajectories there so that, on average, some grains that would have arrived at crests are instead carried over them; in this way crests of *mature* ripples, unlike their stoss or lee sides, are locations where grains are removed as quickly as they arrive (Bagnold, 1941, pp. 151–152).

In addition to the mechanism proposed by Bagnold, wind dynamic pressure might control ripple height also by mechanisms involving increased rolling or increased probability of direct mobilization of grains at crests (Manukyan & Prigozhin, 2009). Ripple growth upward could become more difficult when probability at crests becomes higher than elsewhere along the ripple profile for turbulent eddies to lengthen grain roll-out distances or even initiate short rolling grain movements. Turbulent eddies impose transient wind speed variations as they sweep past, even in settings where (time-averaged) u_* remains constant. Standard deviations of turbulence-related wind speed variations increase linearly with u_* (Panofsky & Dutton, 1984, pp. 159–160). On Earth, where $u_{*\mathrm{ti}}$ is within 20% of $u_{*\mathrm{tf}}$, increases in u_* above the Bagnold focus in a saltation cloud might allow turbulent eddies periodically to penetrate downward on to exposed crestal surfaces (more than troughs) with enough transient shear stress to directly mobilize grains (e.g., by rolling, or by increasing roll-out distances of grains already in motion). At higher u_*, more energetic turbulent eddies would be more likely not just to halt further crest height growth, but to degrade exposed ripple crests during migration, and this would be consistent with ripple crests in well-sorted sands flattening and disappearing at high u_* (Bagnold, 1941, pp. 151; Sharp, 1963; Walker, 1981, pp. 142–145).

Despite the possibilities above, the exact, underlying mechanisms by which wind dynamic pressure limits impact ripple height have received relatively little attention and are not precisely known. They could include a combination of the mechanisms discussed above, possibly with relative contributions between them changing as a function of u_* and grain size. In any case, accounting for the overall effect of wind dynamic pressure on ripple height seems necessary to explain how aeolian impact ripples evolve under constant wind conditions to an ultimate, stable height and wavelength. For example, recent state-of-the-art numerical experiments (Durán et al., 2014) that use the same boundary layer wind profile at ripple crests as at troughs successfully replicate many important aspects of ripple development, but without greater wind dynamic pressure across crests compared with troughs, ripple height continues to grow without stabilizing, even after wavelength stabilizes (Figure S1 of Durán et al., 2014); on the other hand, numerical experiments that account for locally increased shear stress τ at ripple crests, which affects grain exchange between the surface and saltation cloud as well as roll-out lengths of splashed grains, result in ripple height and wavelength eventually stabilizing with time (Manukyan & Prigozhin, 2009).

We interpret reports of impact ripple morphometry varying with u_* and grain sorting to be manifestations of how wind dynamic pressures constrain ripple crest heights, supporting Bagnold's concept. On Earth, Ripple Index ($\mathrm{RI} = \lambda/h$) values of 10–25 are common for aeolian impact ripples of all sizes, including megaripples, but RI values higher than this (i.e., flatter ripple shapes) are typical of well-sorted dune sands and/or higher formative u_* (e.g., Bagnold, 1941, pp. 151–152; McKenna Neuman & Bédard, 2016; Schmerler et al., 2016; Sharp, 1963; Walker, 1981, pp. 142–145). Bagnold, for instance, reported high RI of 30–70 while working with well-sorted dune sands; surface relief was so low in some instances that only glancing illumination was able to reveal the presence of ripples (Bagnold, 1937, 1941, pp. 151–152). Some grain size variation is still present even in the most well-sorted natural sands, and on the basis of his experience Bagnold was perhaps the first to wonder how impact ripples might form, if at all, in a hypothetical sand composed only of truly identically sized grains (Bagnold, 1937, p. 431). Impact ripples with high RI values in well-sorted sands, versus lower RI ripples in less sorted sands, indicate that grain size *contrast* within a sand supply, and the

relative abundance of the coarser-than-average grains, are contributing factors along with wind dynamic pressure for determining mature ripple relief and wavelength. Bagnold and Walker reported complete ripple flattening at highest u_* of their respective experiments, but Schmerler et al. (2016) did not; we attribute this to Schmerler et al. (2016) using sands less sorted (i.e., more abundant coarser grains to maintain crests at higher u_*) than those in Walker's experiments, which were laboriously sieved to provide very well-sorted sand test beds. (We are not aware of grain size-frequency information for Bagnold's high RI ripple experiments.) Wavelength has been observed to increase with increasing u_* (e.g., Andreotti et al., 2006; Rasmussen et al., 2015; Schmerler et al., 2016; Walker, 1981), but there appears to be no consensus explanation for this. Perhaps ripple crests can resist increased wind dynamic pressures at higher u_* only if the coarser-than-average grains available within a deposit are concentrated for more effective protection over fewer crests per area, thus requiring longer wavelengths between. At even higher, excessive u_*, perhaps distributing the same population of available coarser-than-average grains over even fewer crests per area is too dynamically difficult, is no longer sufficiently protective, and/or causes too great a separation between crests for mutual aerodynamic protection among them to be effective, so the ripples are erased.

Appendix B: Numerical experiments methods

The two-dimensional model of sand transport is based on the Exner equation, which expresses mass conservation:

$$\left(1-\lambda_{\mathrm{p}}\right)\rho_{\mathrm{p}}\frac{\partial h}{\partial t}=-\frac{\partial Q}{\partial x} \tag{B1}$$

where $h(x,t)$ is local height of the bed at point x and time t, λ_{p} is the porosity of the bed (adopted value 0.35), ρ_{p} is the grain density, and $Q(x,t)$ is the sand flux, measured per unit width perpendicular to flow, which includes both saltation flux (Q_{s}) and reptation flux (Q_{r}) (Anderson, 1987; Yizhaq et al., 2004, 2014). The model also assumes saltation flux descends toward the bed uniformly and homogeneously (i.e., $\partial Q/\partial x = 0$), only providing energy to splash grains in reptation during grain rebound, therefore not contributing mass locally to the bed for ripple development.

The reptation flux Q_{r} at position x and time t is expressed by the sum of all reptating grains passing through position x at time t. These grains have a probability distribution of reptation path lengths $p(\alpha)$ which depends mainly on grain size (Yizhaq et al., 2014). The reptation flux is given by a double integral term that (extending the approach of Anderson, 1987) transforms Equation B1 into:

$$Q_r^0=mn\int_0^{\infty}p(\alpha)\mathrm{d}\alpha\int_{x-\alpha}^{x}N_{im}(x)\mathrm{d}x \tag{B2}$$

where Q_r^0 is the repation flux on a flat bed, m is the mass of each particle (assumed to be spheres of uniform size and density), n is the average number of reptating grains per impact of one saltating grain, and $N_{\mathrm{im}}{}^0$ is the number density of saltating impacts on a level surface ($\mathrm{m}^{-2}\,\mathrm{s}^{-1}$). Although the descent angle ϕ of actual saltating grains varies (e.g., Schmerler et al., 2016), for simplicity we assume spatial uniformity of the saltation flux and constant ϕ, which allows the number density of impacting grains $N_{\mathrm{im}}(x)$ to depend only on changes in the bed slope h_x (where $h_x = \partial h/\partial x$ or $\tan\theta$ where θ is the local slope of the bed/ripple surface). From geometrical considerations (Yizhaq et al., 2014):

$$N_{\mathrm{im}}(x)=N_{\mathrm{im}}^0\frac{1+h_x\cot\phi}{\sqrt{1+h_x{}^2}} \tag{B3}$$

Equation B3 is inapplicable wherever the ripple lee slope is steeper than the saltating grain descent angle ϕ (i.e., where $1 + h_x \cot\phi < 0$), so impact flux for this case is constrained to be zero, consistent with a leeside shadow zone defined as unreachable by direct saltation flux (e.g., Anderson, 1990; Manukyan & Prigozhin, 2009; Prigozhin, 1999). Saltating grain impacts splash grains on the bed into reptation trajectories and also induce local vibrations causing yet other grains to creep downslope (Hardisty & Whitehouse, 1988). Additionally, local slope is likely to affect final roll-out of reptating grains as they come to rest (e.g., Anderson, 1990; Manukyan & Prigozhin, 2009; Prigozhin, 1999). Both of these gravitational

Table B1
COMSALT Fitted Constants Describing Reptation Lengths

Grain size (μm)	N_{im}^{0} [$m^{-2}s^{-1}$]	n	$p(\alpha)$
200	4,594,302	1.4365	a = 0.000399 b = 0.231 c = 0.0205 s = 1.99399

mechanisms act to somewhat retard reptation flux on the windward slope and increase it on the lee slope, compared with purely geometric slope effects described by Equations B2 and B3. Equation B2 was modified to adjust local reptation flux for these gravitational effects:

$$\frac{\partial h}{\partial t} = -\frac{1}{\rho_p(1-\lambda_p)}\frac{\partial}{\partial x}\left[(1-\mu h_x)\, Q_r^0\right] \tag{B4}$$

where the parameter μ heuristically includes slope-sensitive, gravity-related corrections to the reptation flux discussed above (adopting $\mu = 0.839$ following Yizhaq et al. (2014), although $0.6 < \mu < 1$ does not change results significantly).

The parameters $N_{im}{}^{0}$, n, and $p(\alpha)$ in the ripple model are provided by the saltation model COMSALT (Kok & Renno, 2009), which simulates steady-state saltation in planetary environments (e.g., Kok, 2010a, 2010b). COMSALT results also can contribute inputs to other numerical analyses (e.g., Sullivan & Kok, 2017; Yizhaq et al., 2014). COMSALT numerically models trajectories of saltating particles according to boundary layer properties, grain characteristics, and gravity. Capabilities for modeling the impact splash process and the effects of turbulence on grain trajectories compare well with laboratory results documenting these phenomena (Kok & Renno, 2009). COMSALT also reproduces the value of the impact threshold u_{*ti} and other important characteristics of steady-state saltation clouds (Kok, 2010a). COMSALT results here incorporate the same treatment of Lagrangian turbulence coherence time scale T_L utilized by Yizhaq et al. (2014) for Martian settings.

In preparation for numerical ripple experiments, a series of COMSALT experiments characterized Martian steady-state saltation cloud characteristics at a range of u_* for 200 μm basalt grains. This size falls within the range observed for very large ripples: exposures in wheel trench walls indicate 50–150 μm grains are volumetrically the most abundant size fraction within very large ripples at Gusev and Gale craters, while somewhat coarser surface grains typify crests (200–300 μm at Gusev, commonly ~400 μm at Gale) (Sullivan et al., 2008; Weitz et al., 2018). COMSALT results for reptation lengths have a probability distribution $p(\alpha)$ that can be described using

$$p(\alpha) = s\left(1 - e^{-\sqrt{\frac{x}{a}}}\right)\left(\frac{b}{x}\right)e^{-\sqrt{\frac{x}{c}}} \tag{B5}$$

where a, b, and c are fitted constants, and the constant s is set such that $\int_{\alpha_{min}}^{\alpha_{max}} p(\alpha)d\alpha = 1$ (Table B1). For numerical efficiency, we thus truncate the probability distribution to only account for reptation hops with length between α_{min} and α_{max}; we take $\alpha_{min} = 100$ μm based on the grain scale, and we take $\alpha_{max} = 0.1$ m because simulations results indicate that longer reptation hops are very unlikely. Figure 8 shows $p(\alpha)$ for Martian saltation with $D = 200$ μm diameter grains and eight shear velocities. As in previous work (Ho et al., 2014; Ungar & Haff, 1987; Yizhaq et al., 2014), we find that the probability distribution of the reptation length does not depend on wind shear velocity. Because the probability distribution of reptation length $p(\alpha)$ is independent of u_*, the reptation flux Q_r depends on the impact rate, the number of ejected particles, and of course the specific location along the ripple.

In the ripple development simulations, Equation B4 was solved numerically using the method of Yizhaq et al. (2014) in which an explicit second-order finite difference scheme was utilized with periodic boundary conditions. Integral terms of Equation B4 were calculated using the composite trapezoid rule, and time integration was performed using the second-order Adams-Bashforth rule (Fausett, 1999, pp. 423–424).

Appendix C: Clarification: ripple crest grain sizes at Namib dune

Lapotre et al. (2016) report grain size characteristics of Martian large ripples, based on data from the MSL Sols 1,221–1,244 rover position along the margin of Namib dune (location in Figure 5a). Notably, they reported "no significant grain-size differences between the small and large ripples (Fig. 1, E and F)" (Lapotre et al., 2016, p. 56). The actual large ripple examined closely by the rover that would support this claim is not identified, but Figure 1D of that paper includes a pointer directed toward its location out of the field of view. A review of all MSL data at that location, however, reveals the "large ripple" of

Figure 1D unfortunately was misidentified, indicating a source of confusion that is addressed and clarified here for future studies.

For context, Figures 5b–5d and C1a show color contrasts corresponding to grain size variations between crests and troughs throughout the extensive field of large ripples covering the top of Namib Dune. Figure C1 indicates that the dune margin allowed rover access only to smaller bedforms than these, with color properties indicating lower abundance of >150 μm grains. These bedforms are not representative (in size or color properties) of the extensive ripple field covering the top of Namib dune. Unfortunately, even one of these smaller ripple crests along the dune margin proved impossible to inspect closely, because the only example that might have been reachable by the rover arm was inadvertently rolled over and destroyed by the rover's right front wheel as the rover first drove into position on Sol 1,221, prior to all arm-related investigations (Figure C1). Consequently, Figures 1E and 1F of Lapotre et al. (2016) actually show part of a field of small, $\lambda \sim 10$ cm impact ripples, along with a low-relief terminating end fragment of what was once a larger bedform crest. Figure C1 shows this location is beside, not on, a formerly-larger ripple crest that was once ~12 cm high (Profile b-b′ in Figure 9 of Ewing et al. (2017)) before it was crushed by the rover wheel. The small ripple relief in the MAHLI views of Figure C1 is dominated by 100–150 μm grains, consistent with the very similar, <2 mm high "Otavi" ripple less than 1 m away (location and grain size-frequency information in Figures 10–12 of Sullivan and Kok (2017)). In summary, grain size characteristics in Figures 1E–1F of Lapotre et al. (2016) represent well the smallest type of impact ripples at Namib, but do not inform about grain sorting characteristics of the prominent very large ripples extensively covering the top of Namib dune.

Appendix D: Correlation between grain size and color properties

At Gale crater, on the surfaces of relatively dust-free, large aeolian bedforms, MAHLI images reveal an important, useful correlation between aeolian-sorted grain size, and color. Finer-grained ripple trough materials are more reddish than coarser-grained crests. This correlation manifests also in close-range Mastcam-100 images (ground resolutions ~170 μm/pixel within 2.3 m of the camera, then degrading outward): At larger ripples, close-range Mastcam-100 images typically resolve some of the coarsest crest grains, but none of the more reddish-tinted materials in troughs, whereas smaller ripples of uniform color display no resolved grain size contrasts between crests and troughs (Figure D1). Overall, we have found the correlation between color contrasts and grain size to be consistent for relatively dust-free ripples all along the MSL traverse in MAHLI and Mastcam data (as of Sol 2,800 of the MSL mission). We could not find any examples where this correlation fails; that is, we know of no exceptions in relatively dust-free, active sands where a contrary grain size-color relationship is displayed, or where ripples of uniform color have markedly different dominant grain sizes at crests versus troughs, or where ripples with colors contrasting between crests and troughs actually have the same grain size-frequencies at both places. Analysis of ChemCam (Maurice et al., 2012; Wiens et al., 2012) passive spectra with multispectral Mastcam data explains this grain size-color correlation as deriving from more abundant ferric materials at finer grain sizes versus greater proportions of ferrous materials composing coarser grains (Ehlmann et al., 2017; Johnson et al., 2017, 2018).

Limitations of the grain size-color correlation should be kept in mind, however. First, to be clear, coarser grains are not simply all different in color from finer grains. MAHLI images of relatively dust-free sands show that any particular grain of any size can be nearly any color (e.g., Figures 3–5 of Ehlmann et al., 2017), so the relationship between grain size and color in dust-free ripple sands at Gale is apparent only because (1) average properties of large numbers of grains are involved, and (2) aeolian processes have, in places like ripple crests and troughs, partly segregated grains according to size, allowing the greater proportion of more reddish grains at finer sizes to be revealed at macroscopic scales (cf. Bagnold, 1941, p. 152; cf. McKenna Neuman & Bédard, 2016). Second, specific grain size information from color trends is limited. For example, a smoothly changing continuum of average color with increasing grain size would be ideally informative, but is not indicated, nor can a specific grain size be identified at which change in average color is most abrupt. These points are illustrated by color properties of sands that were scooped by the MSL rover from the margin of Namib dune, sieved on board through 1,000 and 150 μm meshes, then deposited onto the ground into four separate piles representing different size-fractions: <150; >150; 150–1,000; and >1,000 μm. The <150 μm materials were more reddish than the three piles composed of materials >150 μm, and there was little color difference between the >150, 150–1,000, and >1,000 μm piles (Johnson et al., 2017) (Figure 14). Third, the applicability of the grain size-color correlation is discussed

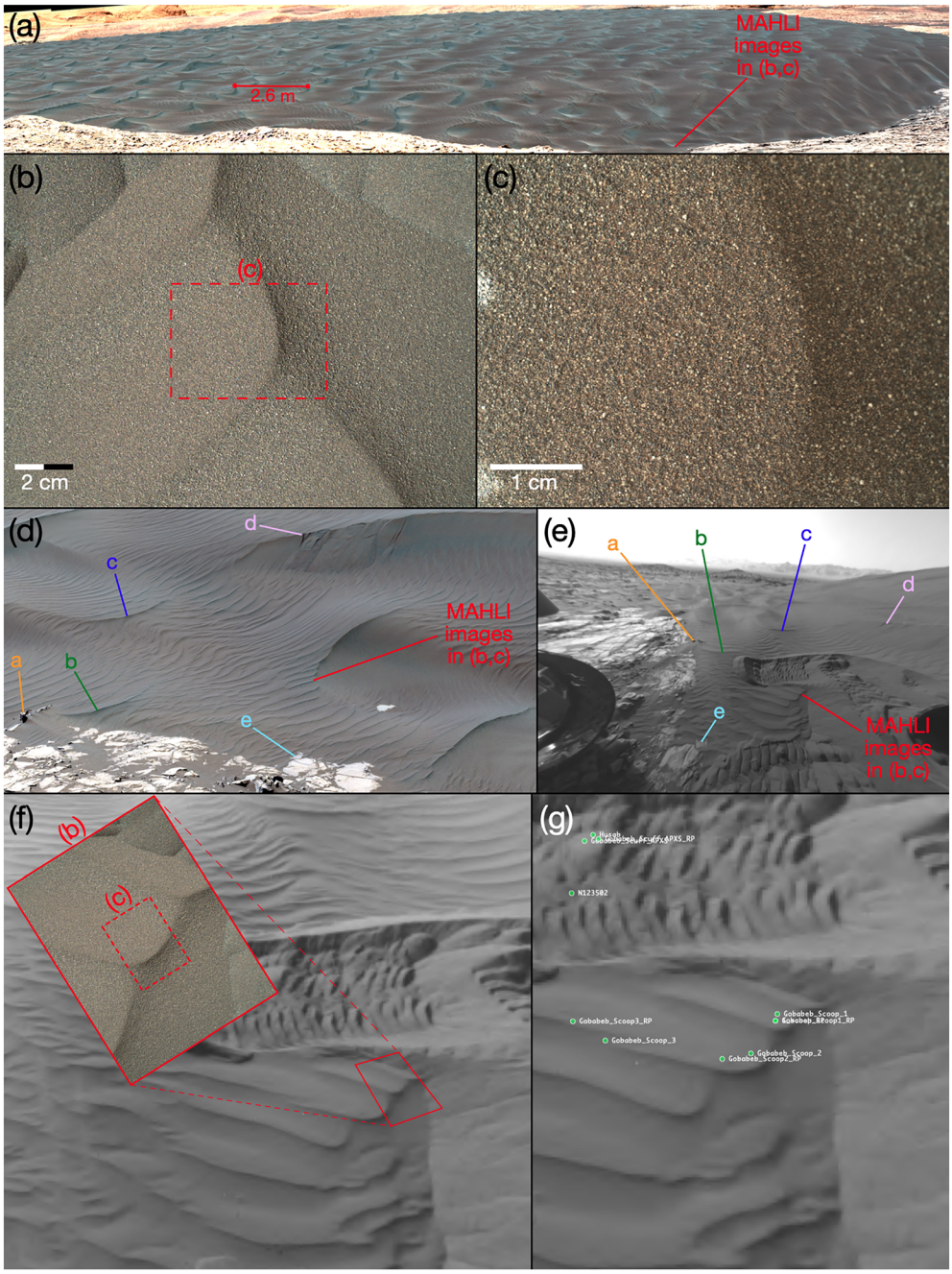

Figure C1. Locating the MAHLI images of Figures 1E and 1F of Lapotre et al. (2016). (a) MSL Sol 1,173 view of Namib dune showing large ripples covering the top surface. For reference, $\lambda = 2.6$ m example is the same location as shown in Figure 5d. In contrast, the dune margin (lower right) where the MAHLI images were obtained has smaller ripples with less extensive zones dominated by >150 μm grains. (Color-stretched mcam05311.) (b, c) The same two MAHLI images of Figures 1E and 1F of Lapotre et al. (2016), displayed in the same side-by-side arrangement. (MAHLI Sol 1,223, 1223MH0005550010403094 and 1223MH0005560010403097.) (d–f) localization of these MAHLI images based on Sol 1,221 predrive Mastcam sequence mcam05597, and Sol 1,221 postdrive Front Hazcam sequence fhaz00302. The larger ripple was accidentally destroyed during the final stages of the Sol 1,221 drive. The MAHLI images were obtained beside what was once the crest of the larger ripple. (g) Screenshot of MSLICE flight operations software confirming the target location of the MAHLI images, which characterized the surface preparing for the first arm-scooping location at the "Gobabeb" site (i.e., at the Sols 1,221–1,244 rover position).

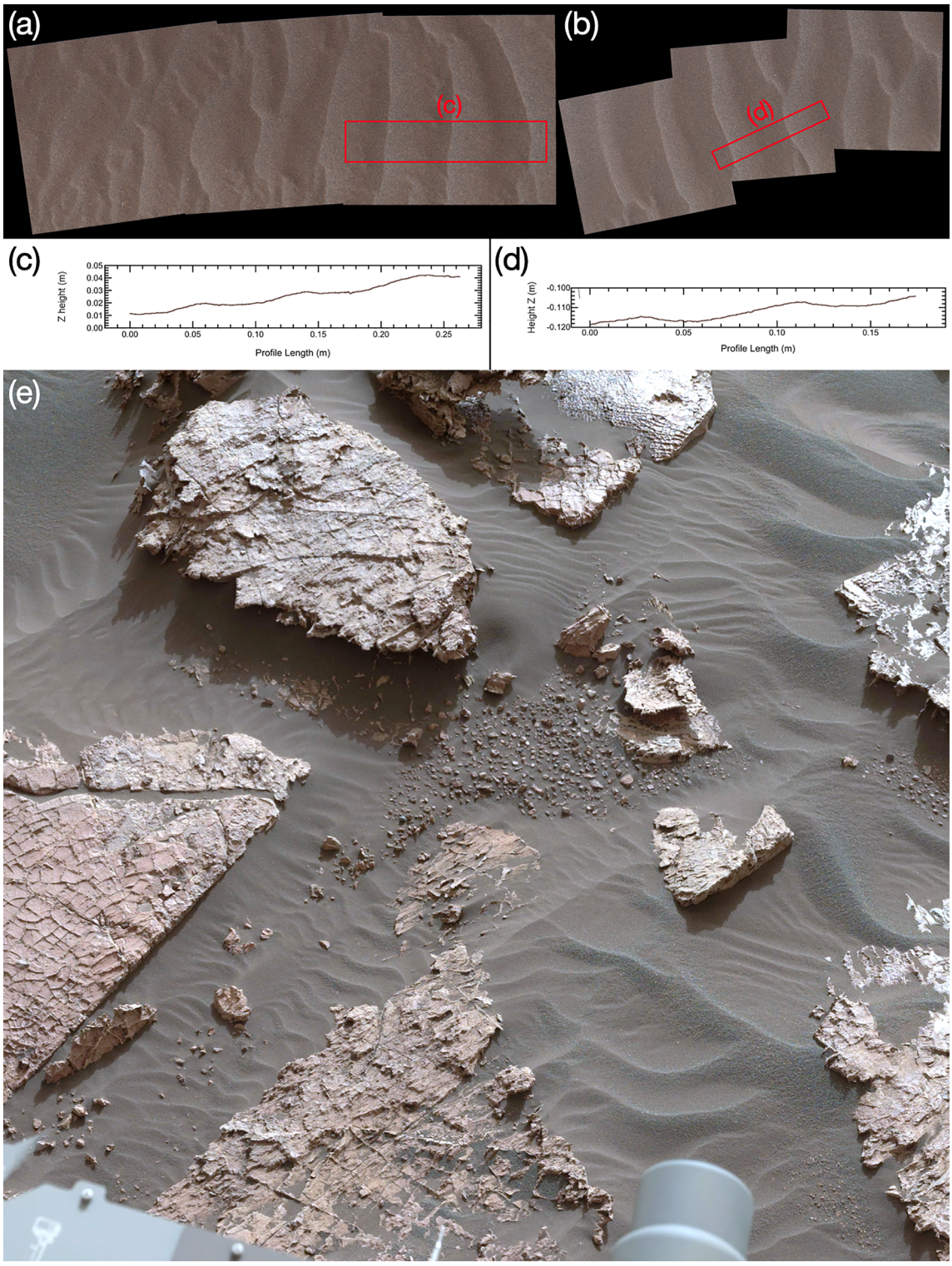

Figure D1. Mastcam images showing correlation between ripple color and grain size. (a–d) Small ripples of uniformly reddish materials have no resolved grains at crests (or troughs). Red boxes in (a) and (b) correspond to profile data in (c) and (d), respectively, and provide scale. (Sol 1,659 mcam08616 and mcam08617.) (e) Lower angle illumination reveals rougher surface texture of coarser materials at crests (especially right side of image), compared with more reddish, smoother (more uniformly finer) trough materials. Scene ~1.2 m across. (Sol 1,555 mcam07986.)

here in reference to active sands at Gale only, without implications for active sands elsewhere on Mars that could be affected by different site-specific weathering contributions from local materials. Finally, illumination conditions at the time of Mastcam image acquisition affect surface color discriminability, so that real color contrasts between active ripple crests and troughs might not be apparent on surfaces illuminated at higher phase angle ϕ (where ϕ = sun-surface-camera angle) or on surfaces indirectly illuminated (partly shadowed), two situations we avoided in this study.

Data Availability Statement

All MSL and MER spacecraft image data used in this work have been archived for free public access by the NASA Planetary Data System (PDS). Within the PDS, MER image data are available at https://pds-geosciences.wustl.edu/missions/mer/geo_mer_datasets.htm, but are more easily accessed in common image formats through the MER Analyst's Notebook at https://an.rsl.wustl.edu/mer/. MSL image data are available at https://pds-imaging.jpl.nasa.gov/volumes/msl.html, but are accessed more easily in common image formats through the MSL Analyst's Notebook at https://an.rsl.wustl.edu/msl/mslbrowser/an3.aspx. Full-resolution images, grain size-frequency analysis data, and numerical experiment outputs supporting the figures and conclusions of this work have been archived at Sullivan et al. (2020), http://doi.org/10.5281/zenodo.3986903.

Acknowledgments

Portions of this research were funded by the NASA Mars Science Laboratory and Mars Exploration Rover missions through the Jet Propulsion Laboratory and Malin Space Science Systems, and also utilized materials from NASA Mars Fundamental Research Program Grant NNG0GH39G to R.S. Additional support was provided by NASA Outer Planets Research Grant NNX14AR23G to J.F.K. The research reported in this paper was enabled by creative and dedicated efforts of Mastcam and MAHLI support personnel at Malin Space Science Systems, JPL, and elsewhere, particularly Jason Van Beek, Tim Olson, David Harker, Tex Kubacki, Kristen Bennett, Megan Wu, and Jill Krezoski during MSL Sols 1748–1752 operations. This work would not have been possible without the dedicated efforts of hundreds of other engineers and science team members on the MSL and MER missions. Discussions with Raleigh Martin, Michael Lamb, and Thomas Pähtz improved this work. During review, comments by Ralph Lorenz and a second anonymous reviewer substantially improved this paper.

References

Allen, J. R. L. (1982). *Sedimentary structures, their character and physical basis* (Vol. 1). Amsterdam: Elsevier Scientific Publishing.

Anderson, F. S., Greeley, R., Xu, P., Lo, E., Blumberg, D. G., Haberle, R. M., & Murphy, J. R. (1999). Assessing the Martian surface distribution of aeolian sand using a Mars general circulation model. *Journal of Geophysical Research*, *104*(E8), 18,991–19,002. https://doi.org/10.1029/1999JE900024

Anderson, R. S. (1987). A theoretical model for aeolian impact ripples. *Sedimentology*, *34*(5), 943–956. https://doi.org/10.1111/j.1365-3091.1987.tb00814.x

Anderson, R. S. (1990). Eolian ripples as examples of self-organization in geomorphological systems. *Earth Science Reviews*, *29*(1-4), 77–96. https://doi.org/10.1016/0012-8252(0)90029-U

Anderson, R. S., & Anderson, S. P. (2010). *Geomorphology, the mechanics and chemistry of landscapes*. Cambridge: Cambridge University Press.

Anderson, R. S., & Bunas, K. L. (1993). Grain size segregation and stratigraphy in aeolian ripples modelled with a cellular automaton. *Nature*, *365*(6448), 740–743. https://doi.org/10.1038/365740a0

Andreotti, B., Claudin, P., & Pouliquen, O. (2006). Aeolian sand ripples: Experimental study of fully developed states. *Physical Review Letters*, *96*, 028001. https://doi.org/10.1103/PhysRevLett.96.028001

Arvidson, R. E., Anderson, R. C., Bartlett, P., Bell, J. F. III, Blaney, D., Christensen, P. R., et al. (2004). Localization and physical properties experiments conducted by Spirit at Gusev crater. *Science*, *305*(5685), 821–824. https://doi.org/10.1126/science.1099922

Arvidson, R. E., Anderson, R. C., Bartlett, P., Bell, J. F. III, Christensen, P. R., Chu, P., et al. (2004). Localization and physical properties experiments conducted by opportunity at Meridiani Planum. *Science*, *306*(5702), 1730–1733. https://doi.org/10.1126/science.1104211

Arvidson, R. E., Ashley, J. W., Bell, J. F. III, Chojnacki, M., Cohen, J., Economou, T. E., et al. (2011). Opportunity Mars Rover mission: Overview and selected results from Purgatory ripple to traverses to Endeavour crater. *Journal of Geophysical Research*, *116*, E00F15. https://doi.org/10.1029/2010JE003746

Arvidson, R. E., Poulet, F., Morris, R. V., Bibring, J.-P., Bell, J. F. III, Squyres, S. W., et al. (2006). Nature and origin of the hematite-bearing plains of Terra Meridiani based on analyses of orbital and Mars Exploration rover data sets. *Journal of Geophysical Research*, *111*, E12S08. https://doi.org/10.1029/2006JE002728

Arvidson, R. E., Ruff, S., Morris, R. V., Ming, D. W., Crumpler, L., Yen, A., et al. (2008). Spirit Mars rover mission to the Columbia Hills, Gusev crater: Mission overview and selected results from the Cumberland Ridge to Home Plate. *Journal of Geophysical Research*, *113*, E12S33. https://doi.org/10.1029/2008JE003183

Bagnold, R. (1935). The movement of desert sand. *The Geographical Journal*, *85*(4), 342–365. https://doi.org/10.2307/1785593

Bagnold, R. (1936). Movement of desert sand. *Proceeding of Royal Society London, Series A*, *157*(892), 594–620. https://doi.org/10.1098/rspa.1936.0218

Bagnold, R. (1941). *The physics of blown sand and desert dunes*. London: Methuen, subsequently reprinted by others (e.g., 1973 by Chapman & Hall, 2005 by Dover).

Bagnold, R. A. (1937). The transport of sand by wind. *The Geographical Journal*, *89*(5), 409–438. http://www.jstor.org/stable/1786411, https://doi.org/10.2307/1786411

Baker, M. M., Lapotre, M. G. A., Minitti, M. E., Newman, C. E., Sullivan, R., Weitz, C. M., et al. (2018). The Bagnold dunes in southern summer: Active sediment transport on Mars observed by the Curiosity rover. *Geophysical Research Letters*, *45*, 8853–8863. https://doi.org/10.1029/2018GL079040

Balme, M., Berman, D. C., Bourke, M. C., & Zimbelman, J. R. (2008). Transverse aeolian ridges (TARs) on Mars (2008). *Geomorphology*, *101*(4), 703–720. https://doi.org/10.1016/j.geomorph.2008.03.011

Banfield, D., Spiga, A., Newman, C., Forget, F., Lemmon, M., Lorenz, R., et al. (2020). The atmosphere of Mars as observed by InSight. *Nature Geoscience*, *13*(3), 190–198. https://doi.org/10.1038/s41561-020-0534-0

Berman, D., Balme, M., Rafkin, S., & Zimbleman, J. (2011). Transverse Aeolian ridges (TARs) on Mars II: Distributions, orientations, and ages. *Icarus*, *213*(1), 116–130. https://doi.org/10.1016/j.icarus.2011.02.014

Bourke, M., Wilson, S., & Zimbelman, J. (2003). The variability of transverse aeolian ridges in troughs on Mars, *LPSC XXXIV*, abstract #2090, https://www.lpi.usra.edu/meetings/lpsc2003/pdf/2090.pdf

Bridges, N., & Ehlmann, B. (2018). The Mars Science Laboratory (MSL) Bagnold dunes campaign, Phase I: Overview and introduction to the special issue. *Journal of Geophysical Research: Planets*, *123*, 3–19. https://doi.org/10.1002/2017JE005401

Bridges, N. T., Ayoub, F., Avouac, J.-P., Leprince, S., Lucas, A., & Mattson, S. (2012). Earth-like sand fluxes on Mars. *Nature*, *485*(7398), 339–342. https://doi.org/10.1038/nature11022

Bridges, N. T., Geissler, P. E., McEwen, A. S., Thomson, B. J., Chuang, F. C., Herkenhoff, K. E., et al. (2007). Windy Mars: A dynamic planet as seen by the HiRISE camera. *Geophysical Research Letters*, *34*, L23205. https://doi.org/10.1029/2007GL031445

Chamberlin, T. C. (1897). Studies for students: The method of multiple working hypotheses. *Journal of Geology*, *5*(8), 837–848. https://doi.org/10.1086/607980

Cheng, H., Liu, C., Li, J., Liu, B., Zheng, Z., Zou, X., et al. (2018). Experimental study of aeolian sand ripples in a wind tunnel. *Earth Surface Processes and Landforms*, *43*(1), 312–321. https://doi.org/10.1002/esp.4246

Chojnacki, M., & Fenton, L. K. (2017). The geologic exploration of the Bagnold dune field at Gale crater by the curiosity rover. *Journal of Geophysical Research: Planets*, *122*, 2216–2222. https://doi.org/10.1002/2017JE005455

Claudin, P., & Andreotti, B. (2006). A scaling law for aeolian dunes on Mars, Venus, Earth, and for subaqueous ripples. *Earth and Planetary Science Letters*, *252*(1-2), 30–44. https://doi.org/10.1016/j.epsl.2006.09.004

Creyssels, M., Dupont, P., Ould El Moctar, A., Valance, A., Cantat, I., Jenkins, J. T., et al. (2009). Saltating particles in a turbulent boundary layer: Experiment and theory. *Journal of Fluid Mechanics*, *625*, 47–74. https://doi.org/10.1017/S0022112008005491

de Silva, S. L., Spagnuolo, M. G., Bridges, N. T., & Zimbelman, J. R. (2013). Gravel-mantled megaripples of the Argentinean Puna: A model for their origin and growth with implications for Mars. *Geological Society of America Bulletin*, *125*(11-12), 1912–1929. https://doi.org/10.1130/B30916.1

Durán, O., Andreotti, B., & Claudin, P. (2012). Numerical simulation of turbulent sediment transport, from bed load to saltation. *Physics of Fluids*, *24*, 103306. https://doi.org/10.1063/1.4757662

Durán, O., Claudin, P., & Andreotti, B. (2011). On aeolian transport: Grain-scale interactions, dynamical mechanisms and scaling laws. *Aeolian Research*, *3*(3), 243–270. https://doi.org/10.1016/j.aeolia.2011.07.006

Durán, O., Claudin, P., & Andreotti, B. (2014). Direct numerical simulations of aeolian sand ripples. *Proceedings of the National Academy of Sciences of the United States of America*, *111*(44), 15,665–15,668. https://doi.org/10.1073/pnas.1413058111

Duran Vinent, O., Andreotti, B., Claudin, P., & Winter, C. (2019). A unified model of ripples and dunes in water and planetary environments. *Nature Geoscience*, *12*(5), 345–350. https://doi.org/10.1038/s41561-019-0336-4

Edgett, K. S., Yingst, R. A., Ravine, M. A., Caplinger, M. A., Maki, J. N., Ghaemi, F. T., et al. (2012). Curiosity's Mars Hand Lens Imager (MAHLI) investigation. *Space Science Reviews*, *170*(1-4), 259–317. https://doi.org/10.1007/s11214-012-9910-4

Ehlmann, B. L., Edgett, K. S., Sutter, B., Achilles, C. N., Litvak, M. L., Lapotre, M. G. A., et al. (2017). Chemistry, mineralogy, and grain properties at Namib and High dunes, Bagnold dune field, Gale crater, Mars: A synthesis of Curiosity rover observations. *Journal of Geophysical Research: Planets*, *122*, 2510–2543. https://doi.org/10.1002/2017JE005267

Ellwood, J. M., Evans, P. D., & Wilson, I. G. (1975). Small scale aeolian bedforms. *Journal of Sedimentary Petrology*, *45*(2), 554–561. https://doi.org/10.1306/212F6DCA-2B24-11D7-8648000102C1865D

Ewing, R., Swann, C., & Sherman, D. (2018). Thresholds and fluxes: Nathan bridges legacy and recent MARSWIT and HiRISE aeolian science, Geol. Soc. Ameri. annual meeting, Paper 54–10, https://gsa.confex.com/gsa/2018AM/webprogram/Paper324241.html

Ewing, R. C., Lapotre, M. G. A., Lewis, K. W., Day, M., Stein, N., Rubin, D. M., et al. (2017). Sedimentary processes of the Bagnold dunes: Implications for the eolian rock record of Mars. *Journal of Geophysical Research: Planets*, *122*, 2544–2573. https://doi.org/10.1002/2017JE005324

Fausett, L. V. (1999). *Applied numerical analysis using MATLAB*. Upper Saddle River, NJ: Prentice-Hall.

Fenton, L. K., & Michaels, T. I. (2010). Characterizing the sensitivity of daytime turbulent activity on Mars with the MRAMS LES: Early results. *Mars*, *5*, 159–171. https://doi.org/10.1555/mars.2010.0007

Fenton, L. K., Toigo, A. D., & Richardson, M. I. (2005). Aeolian processes in Proctor crater on Mars: Mesoscale modeling of dune-forming winds. *Journal of Geophysical Research*, *110*, E06005. https://doi.org/10.1029/2004JE002309

Foroutan, M., & Zimbelman, J. R. (2016). Mega-ripples in Iran: A new analog for transverse aeolian ridges on Mars. *Icarus*, *274*, 99–105. https://doi.org/10.1016/j.icarus.2016.03.025

Fryberger, S. G., Hesp, P., & Hastings, K. (1992). Aeolian granule ripple deposits, Namibia. *Sedimentology*, *39*(2), 319–331. https://doi.org/10.1111/j.1365-3091.1992.tb01041.x

Geissler, P. E. (2014). The birth and death of transverse aeolian ridges on Mars. *Journal of Geophysical Research: Planets*, *119*, 2583–2599. https://doi.org/10.1002/2014JE004633

Geissler, P. E., & Wilgus, J. T. (2017). The morphology of transverse aeolian ridges on Mars. *Aeolian Research*, *26*, 63–71. https://doi.org/10.1016/j.aeolia.2016.08.008

Gillies, J. A., Nickling, W. G., Tilson, M., & Furtak-Cole, E. (2012). Wind-formed gravel bed forms, Wright Valley, Antarctica. *Journal of Geophysical Research*, *117*, F04017. https://doi.org/10.1029/2012JF002378

Greeley, R., & Iversen, J. D. (1985). *Wind as a geological process on Earth, Mars, Venus, and Titan*. Cambridge: Cambridge University Press. https://doi.org/10.1017/CBO9780511573071

Greeley, R., Leach, R., White, B., Iversen, J., & Pollack, J. (1980). Threshold windspeeds for sand on Mars: Wind tunnel simulations. *Geophysical Research Letters*, *7*(2), 121–124. https://doi.org/10.1029/GL007i002p00121

Greeley, R., Squyres, S. W., Arvidson, R. E., Bartlett, P., Bell, J. F. III, Blaney, D., et al. (2004). Wind-related processes detected by the Spirit rover at Gusev crater, Mars. *Science*, *305*(5685), 810–813. https://doi.org/10.1126/science.1100108

Hardisty, R. J. S., & Whitehouse, J. (1988). Evidence for a new sand transport process from experiments on Saharan dunes. *Nature*, *332*(6164), 532–534. https://doi.org/10.1038/332532a0

Herkenhoff, K. E., Squyres, S. W., Bell, J. F. III, Maki, J. N., Arneson, H. M., Bertelsen, P., et al. (2003). Athena Microscopic Imager investigation. *Journal of Geophysical Research*, *108*(E12), 8065. https://doi.org/10.1029/2003JE002076

Hesp, P. A. (1981). The formation of shadow dunes. *Journal of Sedimentary Petrology*, *51*(1), 101–112. https://doi.org/10.1306/212F7C1B-2B24-11D7-8648000102C1865D

Hesp, P. A., & Smyth, T. A. G. (2017). Nebkha flow dynamics and shadow dune formation. *Geomorphology*, *282*, 27–38. https://doi.org/10.1016/j.geomorph.2016.12.026

Ho, T. D., Valance, A., Dupont, P., & Ould El Moctar, A. (2014). Aeolian sand transport: Length and height distributions of saltation trajectories. *Aeolian Research*, *12*, 65–74. https://doi.org/10.1016/j.aeolia.2013.11.004

Holstein-Rathlou, C., Gunnlaugsson, H. P., Merrison, J. P., Bean, K. M., Cantor, B. A., Davis, J. A., et al. (2010). Winds at the Phoenix landing site. *Journal of Geophysical Research*, *115*, E00E18. https://doi.org/10.1029/2009JE003411

Hugenholtz, C. H., & Barchyn, T. E. (2017). A terrestrial analog for transverse aeolian ridges (TARs): Environment, morphometry, and recent dynamics. *Icarus*, *289*, 239–253. https://doi.org/10.1016/j.icarus.2016.08.010

Hugenholtz, C. H., Barchyn, T. E., & Boulding, A. (2017). Morphology of transverse aeolian ridges (TARs) on Mars from a large sample: Further evidence of a megaripple origin? *Icarus*, *286*, 193–201. https://doi.org/10.1016/j.icarus.2016.10.015

Isenberg, O., Yizhaq, H., Tsoar, H., Wenkart, R., Karnieli, A., Kok, J., & Katra, I. (2011). Megaripple flattening due to strong winds. *Geomorphology*, *131*(3-4), 69–84. https://doi.org/10.1016/j.geomorph.2011.04.028

Iversen, J. D., & White, B. R. (1982). Saltation threshold on Earth, Mars and Venus. *Sedimentology*, *29*(1), 111–119. https://doi.org/10.1111/j.1365-3091.1982.tb01713.x

Jerolmack, D. J., Mohrig, D., Grotzinger, J. P., Fike, D. A., & Watters, W. A. (2006). Spatial grain size sorting in eolian ripples and estimation of wind conditions on planetary surfaces: Application to Meridiani Planum, Mars. *Journal of Geophysical Research*, *111*, E12S02. https://doi.org/10.1029/2005JE002544

Johnson, J. R., Achilles, C., Bell, J. F. III, Bender, S., Cloutis, E., Ehlmann, B., et al. (2017). Visible/near-infrared spectral diversity from in situ observations of the Bagnold Dune Field sands in Gale Crater, Mars. *Journal of Geophysical Research: Planets*, *122*, 2655–2684. https://doi.org/10.0002/2016JE005187

Johnson, J. R., Bell, J. F. III, Bender, S., Cloutis, E., Ehlmann, B., Fraeman, A., et al. (2018). Bagnold dunes campaign 2: Visible/near-infrared spectroscopy of longitudinal ripple sands. *Geophysical Research Letters*, *45*, 9480–9487. https://doi.org/10.1029/2018GL079025

Johnston, H. L., & McCloskey, K. E. (1940). Viscosities of several common gasses between 90°K and room temperature. *The Journal of Physical Chemistry*, *44*(9), 1038–1058. https://doi.org/10.1021/j150405a004

Katra, I., Yizhaq, H., & Kok, J. F. (2014). Mechanisms limiting the growth of aeolian megaripples. *Geophysical Research Letters*, *41*, 858–865. https://doi.org/10.1002/2013GL058665

Kok, J. (2010a). Difference in the wind speeds required for initiation versus continuation of sand transport on Mars: Implications for dunes and dust storms. *Physical Review Letters*, *104*, 074502. https://doi.org/10.1103/PhysRevLett.104.074502

Kok, J. (2010b). An improved parameterization of wind-blown sand flux on Mars that includes the effect of hysteresis. *Geophysical Research Letters*, *37*, L12202. https://doi.org/10.1029/2010GL043646

Kok, J. F., Parteli, E. J. R., Michaels, T. I., & Bou Karam, D. (2012). The physics of wind-blown sand and dust. *Reports on Progress in Physics*, *75*, 106901. https://doi.org/10.1088/0034-4885/75/10/106901

Kok, J. F., & Renno, N. O. (2009). A comprehensive numerical model of steady state saltation (COMSALT). *Journal of Geophysical Research*, *114*, D17204. https://doi.org/10.1029/2009JD011702

Laesecke, A., & Muzny, C. D. (2017). Reference correlation for the viscosity of carbon dioxide. *Journal of Physical and Chemical Reference Data*, *46*, 013107. https://doi.org/10.1063/1.4977429

Lämmel, M., Meiwald, A., Yizhaq, H., Tsoar, H., Katra, I., & Kroy, K. (2018). Aeolian sand sorting and megaripple formation. *Nature Physics*, *14*(7), 759–765. https://doi.org/10.1038/s41567-018-0106-z

Lancaster, N. (2009). Dune morphology and dynamics. In A. J. Parsons, & A. D. Abrahams (Eds.), *Geomorphology of desert environments* (pp. 557–595). Dordrecht, Netherlands: Springer. https://doi.org/10.1007/978-1-4020-5719-9_18

Lapotre, M. G. A., Ewing, R. C., Lamb, M. P., Fischer, W. W., Grotzinger, J. P., Rubin, D. M., et al. (2016). Large wind ripples on Mars: A record of atmospheric evolution. *Science*, *353*(6294), 55–58. https://doi.org/10.1126/science.aaf3206

Lapotre, M. G. A., Lamb, M. P., & McElroy, B. (2017). What sets the size of current ripples? *Geology*, *45*(3), 243–246. https://doi.org/10.1130/G38598.1

Lapotre, M. G. A., & Rampe, E. B. (2018). Curiosity's investigation of the Bagnold Dunes, Gale Crater: Overview of the two-phase campaign and introduction to the special collection. *Geophysical Research Letters*, *45*, 10,200–10,210. https://doi.org/10.1029/2018GL079032

Lemmon, E. W., & Jacobsen, R. T. (2004). Viscosity and thermal conductivity equations for nitrogen, oxygen, argon, and air. *International Journal of Thermophysics*, *25*(1), 21–69. https://doi.org/10.1023/B:IJOT.0000022327.04529.f3

Lorenz, R. (1996). Martian surface wind speeds described by the Weibull distribution. *Journal of Spacecraft and Rockets*, *33*(5), 754–756. https://doi.org/10.2514/3.26833

Lorenz, R. D. (2020). Martian Ripples making a Splash. *Journal of Geophysical Research: Planets*, *125*, e2020JE006658. https://doi.org/10.1029/2020JE006658

Lorenz, R. D., & Valdez, A. (2011). Variable wind ripple migration at Great Sand Dunes National Park and Preserve, observed by timelapse imaging. *Geomorphology*, *133*(1–2), 1–10. https://doi.org/10.1016/j.geomorph.2011.06.003

Maki, J., Thiessen, D., Pourangi, A., Kobzeff, P., Litwin, T., Scherr, L., et al. (2012). The Mars Science Laboratory engineering cameras. *Space Science Reviews*, *170*(1-4), 77–93. https://doi.org/10.1007/s11214-012-9882-4

Maki, J. N., Bell, J. F. III, Herkenhoff, K. E., Squyres, S. W., Kiely, A., Klimesh, M., et al. (2003). Mars Exploration Rover engineering cameras. *Journal of Geophysical Research*, *108*(E12), 8071. https://doi.org/10.1029/2003JE002077

Malin, M. C., & Edgett, K. S. (2001). Mars Global Surveyor Mars Orbiter Camera: Interplanetary cruise through primary mission. *Journal of Geophysical Research*, *106*(E10), 23,429–23,570. https://doi.org/10.1029/2000JE001455

Malin, M. C., Ravine, M. A., Caplinger, M. A., Ghaemi, F. T., Schaffner, J. A., Maki, J. N., et al. (2017). The Mars Science Laboratory (MSL) Mast cameras and Descent imager: Investigation and instrument descriptions. *Earth and Space Science*, *4*(8), 506–539. https://doi.org/10.1002/2016EA000252

Manukyan, E., & Prigozhin, L. (2009). Formation of aeolian ripples and sand sorting. *Physical Review E*, *79*, 031303. https://doi.org/10.1103/PhysRevE.79.031303

Martin, R. L., & Kok, J. F. (2017). Wind-invariant saltation heights imply linear scaling of aeolian saltation flux with shear stress. *Science Advances*, *3*, e1602569. https://doi.org/10.1126/sciadv.1602569

Maurice, S., Wiens, R. C., Saccoccio, M., Barraclough, B., Gasnault, O., Forni, O., et al. (2012). The ChemCam instrument suite on the Mars Science Laboratory (MSL) rover: Science objectives and mast unit description. *Space Science Reviews*, *170*(1–4), 95–166. https://doi.org/10.1007/s11214-012-9912-2

McKenna Neuman, C., & Bédard, O. (2016). A wind tunnel investigation of particle segregation, ripple formation and armouring within sand beds of systematically varied texture. *Earth Surface Processes and Landforms*, *42*(5), 749–762. https://doi.org/10.1002/esp.4019

Murphy, J. R., Leovy, C. B., & Tillman, J. E. (1990). Observations of Martian surface winds at the Viking Lander 1 site. *Journal of Geophysical Research*, *95*(B9), 14,555–14,576. https://doi.org/10.1029/JB095iB09p14555

Namikas, S. L. (2003). Field measurement and numerical modelling of aeolian mass flux distributions on a sandy beach. *Sedimentology*, *50*(2), 303–326. https://doi.org/10.1046/j.1365-3091.2003.00556.x

Newman, C., Gómez-Elvira, J. G., Marín, M., Navarro, S., Torres, J., Richardson, M. I., et al. (2017). Winds measured by the Rover Environmental Monitoring Station (REMS) during the Mars Science Laboratory (MSL) rover's Bagnold Dunes Campaign and comparison with numerical modeling using MarsWRF. *Icarus*, *291*, 203–231. https://doi.org/10.1016/j.icarus.2016.12.016

Pähtz, T., Kok, J. F., & Hermann, H. J. (2012). The apparent roughness of a sand surface blown by wind from an analytical model of saltation. *New Journal of Physics*, *14*, 043035. https://doi.org/10.1088/1367-2630/14/4/043035
Pähtz, T., Kok, J. F., Parteli, E. J. R., & Herrmann, H. J. (2013). Flux saturation length of sediment transport. *Physical Review Letters*, *111*, 218002. https://doi.org/10.1103/PhysRevLett.111.218002
Pähtz, T., Valyrakis, M., Zhao, X., & Li, Z. (2018). The critical role of boundary layer thickness for the initiation of aeolian sediment transport. *Geosciences*, *8*, 314. https://doi.org/10.3390/geosciences8090314
Panofsky, H. A., & Dutton, J. A. (1984). *Atmospheric turbulence*. New York: John Wiley & Sons.
Pelletier, J. D. (2009). Controls on the height and spacing of eolian ripples and transverse dunes: A numerical modeling investigation. *Geomorphology*, *105*(3-4), 322–333. https://doi.org/10.1016/j.geomorph.2008.10.010
Pla-Garcia, J., Rafkin, S. C. R., Kahre, M., Gomez-Elvira, J., Hamilton, V. E., Navarro, S., et al. (2016). The meteorology of Gale crater as determined from rover environmental monitoring station observations and numerical modeling. Part I: Comparison of model simulations with observations. *Icarus*, *280*, 103–113. https://doi.org/10.1016/j.icarus.2016.03.013
Prigozhin, L. (1999). Nonlinear dynamics of aeolian sand ripples. *Physical Review E*, *60*(1), 729–733. https://doi.org/10.1103/PhysRevE.60.729
Rasmussen, K. R., Valance, A., & Merrison, J. (2015). Laboratory studies of aeolian sediment transport processes on planetary surfaces. *Geomorphology*, *244*, 74–94. https://doi.org/10.1016/j.geomorph.2015.03.041
Rice, M. A., Willetts, B. B., & McEwan, I. K. (1995). An experimental study of multiple grain-size ejecta produced by collisions of saltating grains with a flat bed. *Sedimentology*, *42*(4), 695–706. https://doi.org/10.1111/j.1365-3091.1995.tb00401.x
Schmeeckle, M. W., Nelson, J. M., Pitlick, J., & Bennett, J. P. (2001). Interparticle collision of natural sediment grains in water. *Water Resources Research*, *37*(9), 2377–2391. https://doi.org/10.1029/2001WR000531
Schmerler, E., Katra, I., Kok, J. F., Tsoar, H., & Yizhaq, H. (2016). Experimental and numerical study of Sharp's shadow zone hypothesis on sand ripple wavelength. *Aeolian Research*, *22*, 37–46. https://doi.org/10.1016/j.aeolia.2016.05.006
Seppälä, M., & Lindé, K. (1978). Wind tunnel studies of ripple formation. *Geografiska Annaler. Series A, Physical Geography*, *60*(1/2), 29–42. https://doi.org/10.2307/520963
Sharp, R. P. (1963). Wind Ripples. *The Journal of Geology*, *71*(5), 617–636. https://doi.org/10.1086/626936
Shockey, K. M., & Zimbelman, J. R. (2013). Analysis of transverse aeolian ridge profiles derived from HiRISE images of Mars. *Earth Surface Processes and Landforms*, *38*, 179–182. https://doi.org/10.1002/esp.3316
Silvestro, S., Vaz, D. A., Ewing, R. C., Rossi, A. P., Fenton, L. K., Michaels, T. I., et al. (2013). Pervasive aeolian activity along rover Curiosity's traverse in Gale Crater, Mars. *Geology*, *41*(4), 483–486. https://doi.org/10.1130/G34162.1
Silvestro, S., Vaz, D. A., Yizhaq, H., & Esposito, F. (2016). Dune-like dynamic of Martian aeolian large ripples. *Geophysical Research Letters*, *43*, 8384–8389. https://doi.org/10.1002/2016GL070014
Siminovich, A., Elperin, T., Katra, I., Kok, J. F., Sullivan, R., Silvestro, S., & Yizhaq, H. (2019). Numerical study of shear stress distribution over sand ripples under terrestrial and Martian conditions. *Journal of Geophysical Research: Planets*, *124*, 175–185. https://doi.org/10.1029/2018JE005701
Soderblom, L. A., Anderson, R. C., Arvidson, R. E., Bell, J. F. III, Cabrol, N. A., Calvin, W., et al. (2004). Soils of Eagle crater and Meridiani Planum at the Opportunity rover landing site. *Science*, *306*(5702), 1723–1726. https://doi.org/10.1126/science.1105127
Spiga, A., & Lewis, S. R. (2010). Martian mesoscale and microscale wind variability of relevance for dust lifting. *Mars*, *5*, 146–158. https://doi.org/10.1555/mars.2010.0006
Sullivan, R., Arvidson, R., Bell, J. F. III, Gellert, R., Golombek, M., Greeley, R., et al. (2008). Wind-driven particle mobility on Mars: Insights from MER observations at "El Dorado" and surroundings at Gusev crater. *Journal of Geophysical Research*, *113*, E06S07. https://doi.org/10.1029/2008JE003101
Sullivan, R., Banfield, D., Bell, J. F. III, Calvin, W., Fike, D., Golombek, M., et al. (2005). Aeolian processes at the Mars Exploration Rover Meridiani Planum landing site. *Nature*, *436*(7047), 58–61. https://doi.org/10.1038/nature03641
Sullivan, R., Golombek, M., Wilson, G., Greeley, R., Kraft, M., Herkenhoff, K., et al. (2000). Results of the imager for Mars pathfinder windsock experiment. *Journal of Geophysical Research*, *105*(E10), 24,547–24,562. https://doi.org/10.1029/1999JE001234
Sullivan, R., & Kok, J. F. (2017). Aeolian saltation on Mars at low wind speeds. *Journal of Geophysical Research: Planets*, *122*, 2111–2143. https://doi.org/10.1002/2017JE005275
Sullivan, R., Kok, J., Katra, I., & Yizhaq, H. (2020). SullivanKokKatraYizhaq_MarsLargeRipples_JGR-Planets_2020JE006485_Archive.tar. https://doi.org/10.5281/zenodo.3986903
Swann, C., Sherman, D. J., & Ewing, R. C. (2020). Experimentally-derived thresholds for windblown sand on Mars. *Geophysical Research Letters*, *47*, e2019GL084484. https://doi.org/10.1029/2019GL084484
Ungar, J. E., & Haff, P. K. (1987). Steady state saltation in air. *Sedimentology*, *34*(2), 289–299. https://doi.org/10.1111/j.1365-3091.1987.tb00778.x
Vaz, D. A., Silvestro, S., Sarmento, P. T. K., & Cardinale, M. (2017). Migrating meter-scale bedforms on Martian dark dunes: Are terrestrial aeolian ripples good analogues? *Aeolian Research*, *26*, 101–116. https://doi.org/10.1016/j.aeolia.2016.08.003
Viúdez-Moreiras, D., Gómez-Elvira, J., Newman, C. E., Navarro, S., Marin, M., Torres, J., et al. (2019a). Gale surface wind characterization based on the Mars Science Laboratory REMS dataset. Part I: Wind retrieval and Gale's wind speeds and directions. *Icarus*, *319*, 909–925. https://doi.org/10.1016/j.icarus.2018.10.011
Viúdez-Moreiras, D., Gómez-Elvira, J., Newman, C. E., Navarro, S., Marin, M., Torres, J., et al. (2019b). Gale surface wind characterization based on the Mars Science Laboratory REMS dataset. Part II: Wind probability distributions. *Icarus*, *319*, 645–656. https://doi.org/10.1016/j.icarus.2018.10.010
Walker, J. D. (1981). An experimental study of wind ripples, M. S. thesis, Department of Earth and Planetary Sciences, Massachusetts Institute of Technology (145 pp.). Retrieved from https://dspace.mit.edu/handle/1721.1/16156
Weitz, C. M., Anderson, R. C., Bell, J. F. III, Farrand, W. H., Herkenhoff, K. E., Johnson, J. R., et al. (2006). Soil grain analyses at Meridiani Planum, Mars. *Journal of Geophysical Research*, *111*, E12S04. https://doi.org/10.1029/2005/JE002541
Weitz, C. M., Sullivan, R. J., Lapotre, M. G. A., Rowland, S. K., Grant, J. A., Baker, M., & Yingst, R. A. (2018). Sand grain sizes and shapes in aeolian bedforms at Gale crater, Mars. *Geophysical Research Letters*, *45*, 9471–9479. https://doi.org/10.1029/2018GL078972
Wiens, R. C., Maurice, S., Barraclough, B., Saccoccio, M., Barkley, W. C., Bell, J. F. III, et al. (2012). The ChemCam instrument suite on the Mars Science Laboratory (MSL) rover: Body unit and combined system tests. *Space Science Reviews*, *170*(1–4), 167–227. https://doi.org/10.1007/s11214-012-9902-4
Williams, J. J., Butterfield, G. R., & Clark, D. G. (1994). Aerodynamic entrainment threshold: Effects of boundary layer flow conditions. *Sedimentology*, *41*(2), 309–328. https://doi.org/10.1111/j.1365-3091.1994.tb01408.x

Wilson, I. G. (1972). Aeolian bedforms—Their development and origins. *Sedimentology*, *19*(3-4), 173–210. https://doi.org/10.1111/j.1365-3091.1972.tb00020.x

Wilson, S., & Zimbelman, J. R. (2004). Latitude-dependent nature and physical characteristics of transverse aeolian ridges on Mars. *Journal of Geophysical Research*, *109*, E10003. https://doi.org/10.1029/2004JE002247

Yang, Y., Liu, L., Shi, P., Zhao, M., Dai, J., Lyu, Y., et al. (2019). Converging effects of shrubs on shadow dune formation and sand trapping. *Journal of Geophysical Research: Earth Surface*, *124*, 1835–1853. https://doi.org/10.1029/2018JF004695

Yizhaq, H., Balmforth, N. J., & Provenzale, A. (2004). Blown by wind: Nonlinear dynamics of aeolian sand ripples. *Physica D*, *195*(3-4), 207–228. https://doi.org/10.1016/j.physd.2004.03.015

Yizhaq, H., & Katra, I. (2015). Longevity of aeolian megaripples. *Earth and Planetary Science Letters*, *422*, 28–32. https://doi.org/10.1016/j.epsl.2015.04.004

Yizhaq, H., Katra, I., Isenberg, O., & Tsoar, H. (2012). Evolution of megaripples from a flat bed. *Aeolian Research*, *6*, 1–12. https://doi.org/10.1016/j.aeolia.2012.05.001

Yizhaq, H., Kok, J. F., & Katra, I. (2014). Basaltic sand ripples at eagle crater as indirect evidence for the hysteresis effect in Martian saltation. *Icarus*, *230*, 143–150. https://doi.org/10.1016/j.icarus.2013.08.006

Zhao, Y., Gao, X., Lei, J., Li, S., Cai, D., & Song, Q. (2019). Effects of wind velocity and nebkha geometry on shadow dune formation. *Journal of Geophysical Research: Earth Surface*, *124*, 2579–2601. https://doi.org/10.1029/2019JF005199

Zimbelman, J. R. (2010). Transverse Aeolian Ridges on Mars: First results from HiRISE images. *Geomorphology*, *121*(1-2), 22–29. https://doi.org/10.1016/j.geomorph.2009.05.012

Zimbelman, J. R., & Scheidt, S. P. (2014). Precision topography of a reversing sand dune at Bruneau dunes, Idaho, as an analog for transverse aeolian ridges on Mars. *Icarus*, *230*, 29–37. https://doi.org/10.1016/j.icarus.2013.08.004